Journal of Volcanology and Geothermal Research 377 (2019) 131–145

Contents lists available at ScienceDirect

Journal of Volcanology and Geothermal Research

journal homepage: www.elsevier.com/locate/jvolgeores

A model for the development of stable isotopic water signatures of tephra deposited on ice following subglacial caldera collapse

Alan W. Rempel*, Ilya N. Bindeman

Department of Earth Sciences, University of Oregon, Eugene, USA

ARTICLE INFO

Article history:
Received 26 November 2018
Received in revised form 13 March 2019
Accepted 25 March 2019
Available online 11 April 2019

Keywords:
Caldera
Hydration
Stable isotopes
Tephra
Yellowstone
Alteration

ABSTRACT

Large-scale silicic volcanism has occurred frequently in regions mantled by thin to very thick glacial ice cover, with several notable examples during the Pleistocene (Yellowstone, Long Valley, Iceland), including high altitude activity during the most recent glacial (e.g. Cascades, Kamchatka, Andes). More ancient caldera-forming events must have occurred during episodes of long-lasting (ca. 10–50 Ma) snowball Earth glaciation in the Neo- and Paleo-proterozoic, and many extraterrestrial eruptions on other ice-covered planets and moons are also of this general form. Recent work suggests that the process of caldera collapse typically lasts hours to weeks, during which the caldera floor drops by several hundreds to thousands of meters and is covered by hot tephra. With this scenario in mind, we investigate glaciovolcanic interactions immediately following the deposition of thick, hot ash layers on ice and consider the destiny of buried tephra and melting ice inside calderas. Our focus is drawn in particular to the post-emplacement hydration of volcanic glasses, with the goal of assessing whether the $\delta^{18}O$, $\delta^{17}O$ and δD signatures in ancient deposits might be used to infer the syn-eruptive climate state. Scaling arguments, augmented by an idealized 1D model, suggest that ice should often survive for several decades or centuries as an active meltwater source to the overlying cooling intracaldera tuff. As liberated glacial water (both liquid and vapor) infiltrates and interacts with the tephra layer, volcanic glasses can become fully hydrated to water saturations of several wt.%. Our theoretical treatment is motivated in part by our recent measurements of lower than modern δD values in products of several Pleistocene eruptions in the western U.S. occupying regions that were likely glaciated immediately prior to the emplacement of volcanic products. We discuss how $\delta^{18}O$–δD and $\delta^{18}O$–$\Delta^{17}O$ systematics can be used to recognize syn-glacially hydrated intracaldera tephra, potentially including samples that have been buried, altered and subsequently exposed either by fault uplift and erosional exposure or by drilling operations, such as those being performed currently in the Central Snake River Plain near Yellowstone.

1. Introduction

Advances in our understanding of glaciovolcanism have benefited from focused efforts to quantify and predict the hazards associated with recent eruptive activity in ice-clad volcanic centers in Iceland and Alaska (e.g. Smellie and Edwards, 2016). Many volcanoes at mid to high latitudes are covered by snow and ice, with modern eruptive activity exposing the varied influences of centimeter- to meter-scale layers of cool ash on glacier ablation (e.g. Barr et al., 2018). Recognizing that caldera volcanoes in particular often host sizable ice caps, in this work we are drawn to consider the more dramatic and rare end-member case in which a thick (i.e. 10s to 100s of meters) layer of hot ash is emplaced upon and melts its way into glacial ice that is impounded during caldera collapse. Our interest is peaked in part by moraine-based reconstructions, alongside many other lines of geomorphological evidence which suggest that subglacial volcanoes and calderas were more numerous during past glacial periods (e.g. Barr and Clark, 2012; Smellie and Edwards, 2016). Indeed, the record of volcanic ash and glacial debris recovered from North Pacific sediment cores that sample material originating in the Kamchatka and Aleutian arcs demonstrates that the frequency of volcanic eruptions during Pleistocene glacial periods was higher than it is today (Kennett and Thunell, 1977; Bigg et al., 2008; Bindeman et al., 2010). Elevated areas in western North America, including the regions surrounding the Yellowstone and Long Valley calderas, retain abundant evidence of past glaciation (i.e., within the Beartooth mountains near Yellowstone and the Sierra Nevada near Yosemite). As a result of overprinting, surficial evidence for only two or three distinct glacial epochs can be identified (Pierce, 2003; Richmond, 1986; Smith and Siegel, 2000), but the marine sediment and $\delta^{18}O$ foraminifera records

* Corresponding author.
E-mail address: rempel@uoregon.edu (A.W. Rempel).

https://doi.org/10.1016/j.jvolgeores.2019.03.015
0377-0273/

(Lisiecki and Raymo, 2005) strongly support the expectation that the past 2.6 Ma has witnessed tens of glacial advances and retreats at these sites. Although ice geometry over the Yellowstone and Long Valley calderas during these past glacial periods is not well constrained, evidence from the most recent glaciation suggests that ice thicknesses likely exceeded several hundred meters (Smith and Siegel, 2000), as illustrated in Fig. 1. Here, we examine whether the rapid hydration of glass particles at elevated temperatures is able to impart recognizable isotopic signatures that might be used to determine the syn-eruptive climate state based on inferred characteristics of the glacial meltwater source.

Despite ample opportunity for major Pleistocene "supervolcanic" caldera-forming eruptions to occur subglacially, clear evidence to discriminate between glacial and interglacial conditions during the most recent events at Yellowstone (Lava Creek tuff: 0.63 Ma, Mesa Falls tuff: 1.3 Ma, Huckleberry Ridge tuff: 2.05 Ma; Wotzlaw et al., 2015; Singer et al., 2014), and Long Valley (Bishop tuff: 0.75 Ma; Crowley et al., 2007) has remained elusive. For example, uncertainties in the Ar–Ar and U–Pb ages reported for the Lava Creek tuff permit an eruption either within maximal glacial conditions or during the MIS15/16 interglacial (Fig. 2), with the 631 ka preferred age (Wotzlaw et al., 2015) placing it during the glacial MIS16. However, Sarna-Wojcicki et al. (1987) found ash from the eruption that formed the Lava Creek tuff in Lake Tecopa in California, attributing it to interglacial conditions. More recently Dean et al. (2015) described a layer of Lava Creek tuff in a bore hole within the Santa Barbara Basin containing foraminiferal constraints that place it within the MIS15/16 interglacial transition. The EPICA ice core in Antarctica extends back some 800 thousand years (Parrenin et al., 2007), which encompasses both the Lava Creek and Bishop tuff eruption ages, but the tephra particles needed to distinguish particular eruptive sources from the Northern Hemisphere are scarce in Antarctic cores and no evidence for these particular events has been identified. Ash from southern hemisphere events, such as those in the ice-covered Andes requires further detailed study including improved dating constraints.

Taking a broader view, the geologic record contains evidence that large caldera-forming eruptions take place at an average of approximately once every 100,000 years (Mason et al., 2004). This frequency suggests that multiple caldera collapses likely happened over the course of the 10–50 million year duration Neo- and Paleoproterozoic Snowball Earth glaciations. Indeed, similar events almost certainly occur on volcanically active planets and moons that are currently mantled by extensive ice cover (e.g. Scott and Tanaka, 1982). Efforts to explore potential connections between eruptive behavior and climate forcing are hampered by the limited resolution of records connecting the timing of eruptions with the contemporary climate state. Absent geomorphological evidence indicating the presence or absence of ice during such volcanic episodes, the hypothesis pursued here is that the climate state may be revealed through close examination of the $\delta^{18}O$, $\delta^{17}O$ and δD signatures that result from rapid post-emplacement hydration of volcanic glasses contained within tephra layers.

The deposition of thick tephra blankets over snow and water-filled valleys has been observed historically (Griggs, 1922; Hildreth and Fierstein, 2012), interpreted in ancient deposits (Sheridan, 1970) and described in numerical models (Keating, 2005). As the hot ash

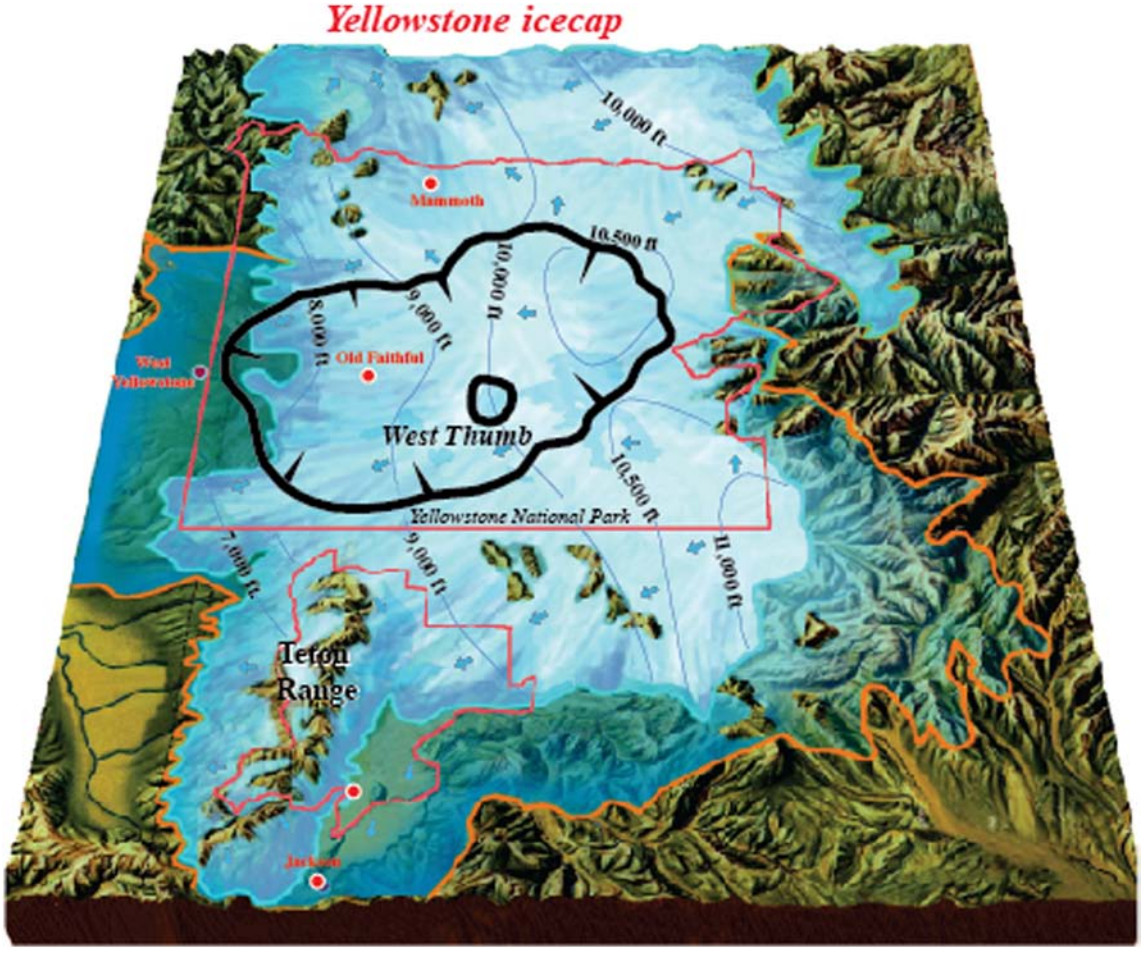

Fig. 1. A reconstruction of the approximate icecap geometry at Yellowstone during the last glacial maximum (~18 ka), with the West Thumb (174 ka) and Yellowstone (630 ka) calderas shown in black (Bob Smith, personal communication 2018).

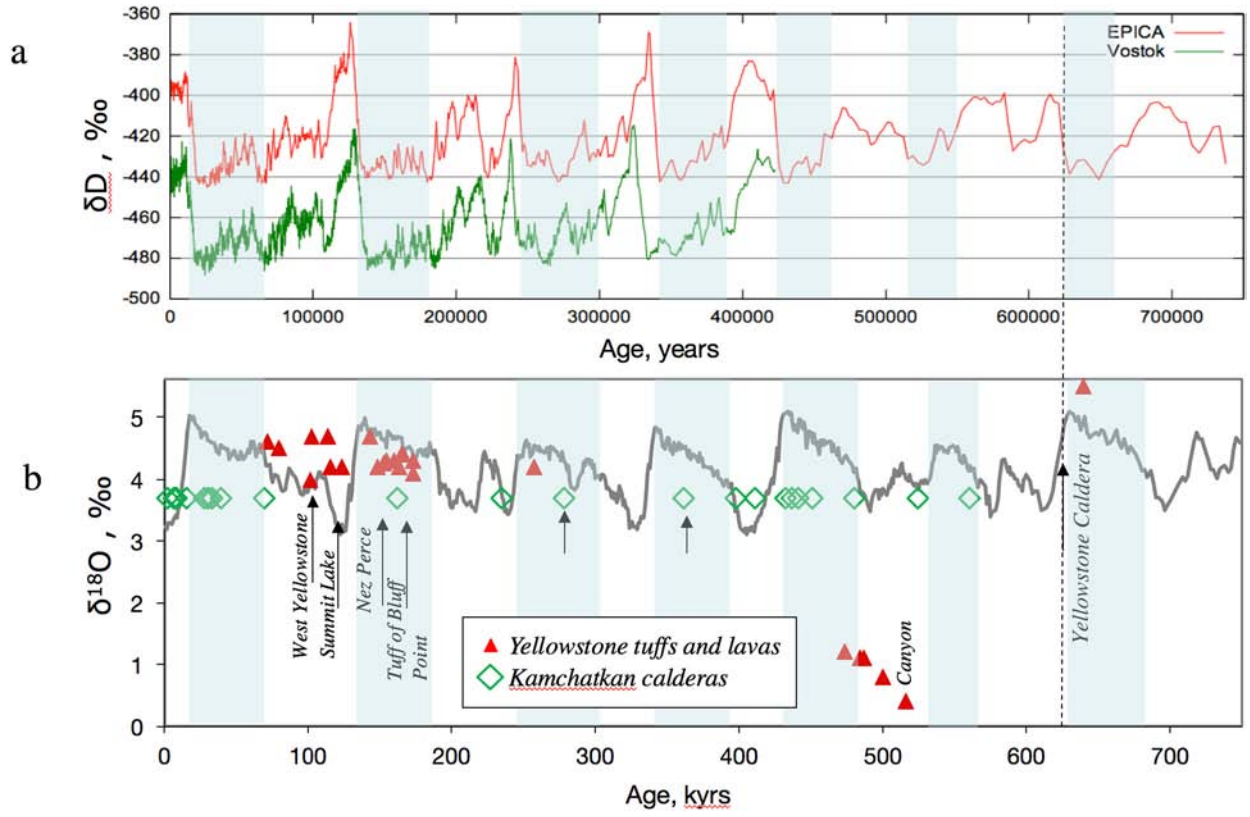

Fig. 2. Ages of Yellowstone eruptions compared to records of global paleoclimate proxies. a) EPICA (Jouzel et al., 2007) and Vostok (Petit et al., 1999) Antarctic ice δD records, with glacial conditions shaded blue (delineated by $\delta^{18}O$ reaching 75% of peak glacial values). b) Foraminiferal sediment record of $\delta^{18}O$ (Lisiecki and Raymo, 2005), with ages of dated Yellowstone eruptions discussed in text (Ar–Ar ages are from Christiansen et al., 2007). Lava Creek tuff of Yellowstone erupted 630 ka, as determined by two independent dating methods Ar-Ar and U-Pb (Wotzlaw et al., 2015; Matthews et al., 2015), and corroborated by correlations observed in marine sediments (Dean et al., 2015). Ages of Yellowstone lavas and tuffs are plotted against their magmatic $\delta^{18}O$ values, which have no relationship with the foraminiferal $\delta^{18}O$ values that are shown with the continuous curve.

cools, thermal fronts propagate downwards and liberate steam that percolates through the tephra before escaping its upper surface. In addition to enhancing the rate of heat transfer, interaction with locally sourced mobile water can produce dramatic shifts to the oxygen and hydrogen isotopic content of the newly deposited volcanic material (Gazis et al., 1996; Holt and Taylor, 2001; Seligman et al., 2018; Hudak and Bindeman, 2018). By extension, although definitive evidence for subglacial caldera collapse events has yet to be presented, we anticipate that such eruptions must commonly result in the rapid burial of ice by tephra and/or lava, immediately followed by vigorous interactions with liquid water and steam. Here, we present an idealized model that is designed to capture the essential processes involved and track the development of oxygen and hydrogen isotopic signatures in glass and alteration products. The aim is to develop intuition for how the water isotopes contained in such deposits might be used to infer the syn-eruptive climate state.

2. Methods

The enrichment in light isotopes of hydrogen and oxygen within glacial ice is diagnostic of the climate conditions during their deposition with surface snow (e.g. Dansgaard et al., 1993; Masson-Delmotte et al., 2008). We strive to determine the degree to which the hydration of volcanic glasses during the cooling of tephra deposited on glaciers can be analyzed to infer the conditions that prevailed during emplacement. We are particularly interested in caldera collapse events, which are typically expected to extend over hours to weeks (Wilson and Hildreth, 1997; Bacon, 1983) and are characterized by the development of extensive ring fractures that cause the ground surface to drop hundreds of meters even as vent activity expels sufficient material to produce intercaldera tephra deposits of comparable thickness. In Section 2.1 we approximate the thermal history of the tephra over the following decades and centuries as it sinks downwards into the melting ice and liberates steam that rises and interacts with glass particles along its path. The temperature-dependent water solubility, diffusivity and fractionation factors conspire to modify the isotopic signature imparted upon the tephra from the glacial water source. In Section 2.2 we describe an idealized model for glass hydration and in Section 2.3 we consider the processes that determine the stable isotopic signatures that characterize these deposits. We discuss the potential to infer past climate conditions from these volcanic records in Section 3 before offering brief concluding remarks.

2.1. Thermal evolution

The extent of post-depositional alteration of tephra depends upon the thermal history. In the scenario we envision, tephra of thickness H_t at initial temperature $T_m + \Delta T$ is deposited on impermeable ice of thickness H_i and constant temperature $T_m \approx 273$ K. Simple scaling arguments are useful for gaining intuition into the expected behavior.

We focus our attention on ice thicknesses that are sufficient to survive the tephra-cooling process, thereby ensuring an ample glacial source of (low δD, $\delta^{18}O$, $\delta^{17}O$) hydrating fluids. For illustration, we choose tephra emplacement temperatures T between 100 and 400 °C, assuming that the tephra cooled somewhat prior to settling in the newly-formed caldera cavity, but our analysis of tephra survival can be extended to higher temperatures as well. When the emplacement temperature exceeds the liquid boiling point $T_v \approx$

373 K, an enthalpy balance argument suggests that with roughly half of the cooling attributed to heat transfer with the ice (the other half is attributed to convective and radiative transfer across the tephra–atmosphere boundary), melting will consume an ice layer of thickness

$$H_m \approx \frac{H_t}{2}\left[\frac{\bar{\rho C}_v\,(T_m + \Delta T - T_v)}{\rho_l L_v + \rho_i L_m} + \frac{\bar{\rho C}_l\,(T_v - T_m)}{\rho_i L_m}\right]. \quad (1)$$

Here, $\bar{\rho C}_v$ and $\bar{\rho C}_l$ represent the volumetric heat capacities of vapor- and liquid-saturated tephra and $\rho_l L_v$ and $\rho_i L_m$ account for the latent heats of vaporization and melting. The first term in brackets approximates the amount of ice that is both melted and vaporized as the tephra cools to the boiling point and the second term describes the further melting needed to reduce the temperature to ambient levels. Substitution of the nominal parameter values from Table 1 suggests that ice availability as a meltwater source should not generally be a limiting factor; at least some glacial ice should survive the cooling process if its thickness exceeds approximately 80% of the tephra thickness when the emplacement temperature is elevated above the melting point by $\Delta T \leq 400^{\circ}$C (see Fig. 3).

An estimate of the time to cool the tephra to ambient levels is also instructive. A small multiple of the time scale for conductive cooling serves as an approximate upper bound, wherein

$$t_k \approx \frac{\bar{\rho C}_l H_t^2}{4k_l}, \quad (2)$$

with k_l representing the liquid-saturated thermal conductivity (liquid-saturated properties are favored for the desired upper bound on cooling duration because vapor-saturated thermal diffusivities are typically higher). A moving boundary between liquid- and vapor-saturated tephra propagates upwards as meltwater infiltrates from below. A lower bound on the cooling time scale can be identified with the duration required for the tephra to become completely saturated with liquid, approximated as

$$t_m \approx \frac{\rho_i L_m n H_t^2}{2k_l \Delta T}, \quad (3)$$

Table 1
Nominal parameter values used to approximate the thermal evolution of tephra deposited on ice. Note: P and T are pressure and temperature; $\tilde{R}$ is the mass-based gas constant for water vapor (e.g. in J kg^{-1} K^{-1}). We note that tephra thicknesses exceeding several tens of meters are observed in several Alaskan locales (e.g. Griggs, 1922; Hildreth and Fierstein, 2012; Miller and Smith, 1987). Rhyolitic eruptive temperatures typically range from 700-800 °C; our assigned nominal emplacement temperature of 240 °C allows for significant atmospheric cooling while avoiding complications associated with welding and the breakdown of glass to form clays.

Parameter (units)	Nominal value
Tephra thickness H_t (m)	100
Ice thickness H_i (m)	1000
Melting temperature T_m (K)	273
Vaporization temperature T_v (K)	373
Ambient temperature T_a (K)	273
Tephra temperature excess ΔT (K)	240
Liquid-sat. heat capacity $\bar{\rho C}_l$ (J m^{-3} K^{-1})	4×10^6
Vapor-sat. heat capacity $\bar{\rho C}_v$ (J m^{-3} K^{-1})	1×10^6
Liquid-sat. conductivity k_l (W m^{-1} K^{-1})	2
Vapor-sat. conductivity k_v (W m^{-1} K^{-1})	1.5
Vapor density ρ_v (kg m^{-3})	$P/(\tilde{R}T)$
Liquid heat capacity $\rho_l C_l$ (J m^{-3} K^{-1})	4×10^6
Vapor heat capacity $\rho_v C_v$ (J m^{-3} K^{-1})	$2P/(5T)$
Latent heat of fusion $\rho_i L_m$ (J m^{-3})	3×10^8
Latent heat of vaporization $\rho_l L_v$ (J m^{-3})	7×10^8
Porosity n	0.4
Boltzmann's constant σ (W m^{-2} K^{-4})	5.67×10^{-8}
Heat transfer coefficient h (W m^{-2} K^{-1})	20

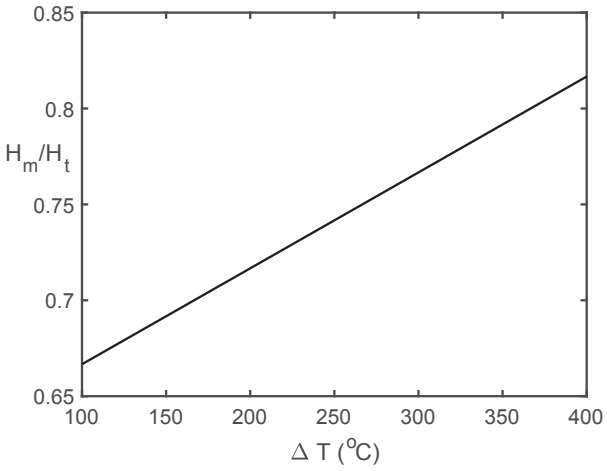

Fig. 3. Ratio of the expected thickness of ice melted during cooling H_m to the tephra thickness H_t, obtained from Eq. (1) with the nominal properties listed in Table 1. Even when emplacement temperatures exceed the melting point by several hundred degrees, the thickness of ice melted is expected to be less than that of the porous tephra.

where n is the tephra porosity. Using the nominal parameters from Table 1, Fig. 4a) shows the conductive time scale from Eq. (2) as a function of tephra thickness, and Fig. 4b) plots the fraction of this time required for melt saturation from Eq. (3) as a function of the emplacement temperature. For example, a tephra layer 100 m thick would be expected to cool by conduction over a characteristic time scale of $t_k \approx 160$ years, and be completely saturated with meltwater in approximately one quarter of this time if $\Delta T \approx 240^{\circ}$C. We are particularly interested in tephra emplacement temperatures below 250 °C, beyond which the glass is expected to breakdown to form clays, precluding our simple hydration treatment; at higher temperatures still, we note that welding is expected to take place and limit the transport of hydrating fluids.

Building upon the intuition gained from these scaling arguments, a more complete mathematical description of the thermal evolution is provided in the Appendix. The predicted behavior is illustrated in Fig. 5 using the nominal parameters from Table 1. Melting is rapid over the first several years as the tephra and ice surfaces subside and a vapor front propagates upwards (Fig. 5a). The temperature profiles (Fig. 5b) change quickly at first, but much more gradually at later times after the entire tephra column becomes saturated with liquid water. The approximately 60 m of melting obtained for this scenario compares reasonably well with the 74 m estimate implied by the scaling argument from Eq. (1) (see Fig. 3). The 24 years needed for liquid to completely saturate the 100 m thick tephra layer is within a factor of two of the 40-year estimate obtained using Eq. (3), and the overall time required to cool to ambient levels falls within the range expected from Eq. (2) (see Fig. 4).

2.2. Compositional evolution

The solubility of H_2O in rhyolite is $C_{sat} \approx 0.1$wt.% at atmospheric pressure and magmatic temperatures (Newman and Lowenstern, 2002). Solubility experiments conducted below the glass transition temperature $T_g \approx 600$–700°C are challenging, but both empirical data and experiments (Friedman et al., 1966; Anovitz et al., 2008) indicate that much higher concentrations of water (e.g. 3.5–4.5 wt.%, Friedman et al., 1993a) are incorporated in rhyolitic glass at 100–250 °C than would be expected by extrapolation of data from temperatures above T_g. Clays form rapidly in the intermediate range of temperatures above about 250 °C and less than T_g; such alteration products can accommodate considerable stores of moisture and are

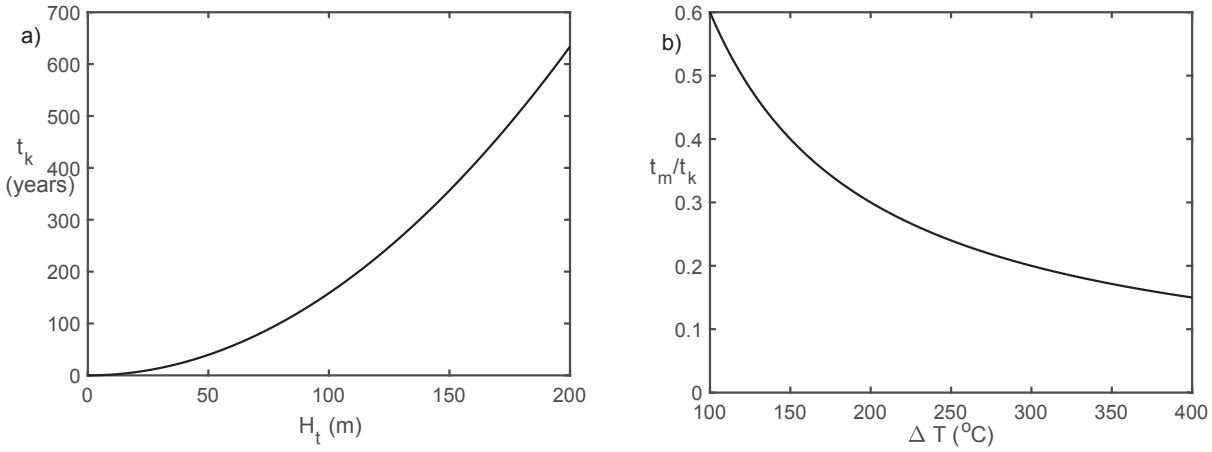

Fig. 4. Time scales for tephra cooling calculated using the nominal parameters from Table 1. a) The conductive time scale from Eq. (2) grows with the square of tephra thickness. b) Fraction of the conductive time scale required for meltwater to saturate the tephra thickness according to Eq. (3). This provides an estimate of the time required for the tephra to cool below the boiling point – since compositional diffusion is most rapid at higher temperatures, this can be viewed as the post-emplacement duration over which significant hydration and isotopic exchange take place.

likely responsible for extreme values in hydration levels, which have been reported to reach as high as 12 wt.% (Anovitz et al., 1999; Tuffen et al., 2010). Nearer to ambient temperatures, the glass itself appears to mainly incorporate molecular H_2O (Anovitz et al., 2004) without much repartition into OH; this behavior is notably distinct from that above T_g, where comparable amounts of dissolved OH and H_2O coexist (Bindeman and Lowenstern, 2016; Seligman et al., 2016; Zhang and Behrens, 2000). For the calculations shown here we assign

$$C_{sat} \approx \left(\frac{1500\ \mathrm{K}}{T} - 1.4\right)\ \mathrm{wt.\%}, \tag{4}$$

which approximates the available observations reasonably well (e.g. Bindeman and Lowenstern, 2016; Friedman et al., 1993b, 1966; Hudak and Bindeman, 2018; Nolan and Bindeman, 2013; Seligman et al., 2016). We note that the thermal dependence implied by Eq. (4) agrees with thermodynamic predictions for an increase in C_{sat} with decreasing temperature (see Duan, 2014). However, we stress the importance of ongoing experimental efforts to better constrain the precise controls on water solubility. In the scenario we envision, hot tephra containing glass particles idealized as spheres of radius a is deposited in a nearly anhydrous state with uniform $C(t = 0) = 0.1$wt.%; subsequent hydration proceeds with the surface concentration $C(r = a, t) = C_0(t) = C_{sat}(T)$ given by Eq. (4), resulting in a gradual increase as T is reduced.

Exchange of water between the surface at $C_0(t)$ and the glass interior takes place by compositional diffusion that is driven by gradients in the chemical potential. Heat transport in glass is much more rapid than compositional transport, so temperature gradients within individual glass particles are sufficiently muted that they do not directly affect compositional (or isotopic) transport. Instead, the transport direction coincides with the direction of steepest decent in water concentration. We note, however, that even after spatially uniform water concentrations are achieved, diffusive exchange can continue to modify the stable isotope content of the dissolved water as long as gradients in δD, δ^{18}O, and δ^{17}O persist. Importantly, the

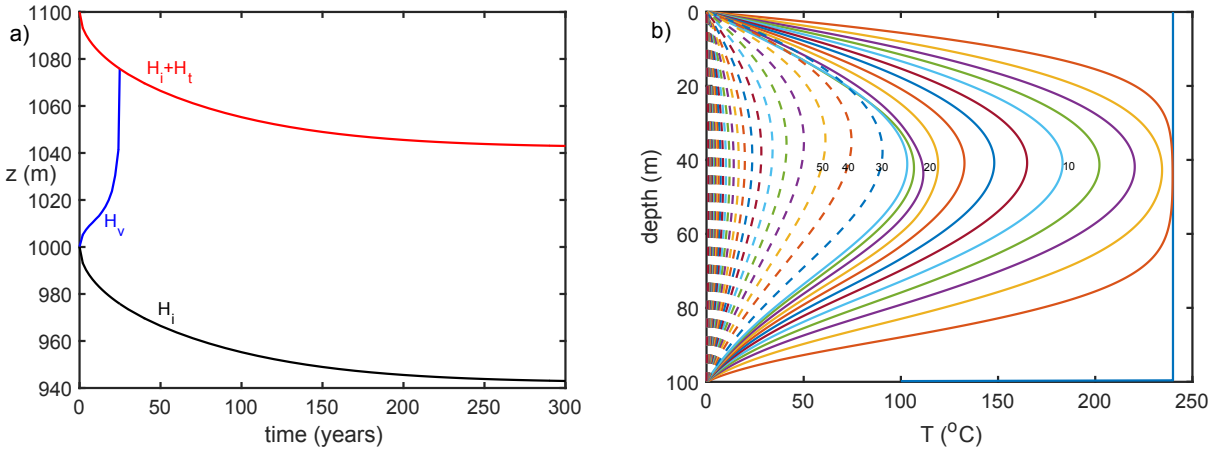

Fig. 5. Thermal evolution of tephra on ice, modeled with the nominal parameters given in Table 1. a) Predicted changes in elevation of the ice surface H_i, the tephra surface $H_i + H_t$ and the interior boundary between liquid- and vapor-saturated tephra H_v. b) Thermal profiles through time, shown with solid lines at successive 2-year increments for the first 24 years during which a vapor-infiltrated zone extends between the tephra surface and H_v. Dashed lines show the more gradual subsequent evolution at 10-year increments.

diffusivity of water in glass changes dramatically with temperature (and also water content) – facilitating relatively rapid hydration shortly after emplacement while the tephra is still hot, followed by essentially negligible alteration over the long time periods that ambient temperatures persist. As discussed further in the Appendix, we approximate this behavior by extrapolating the model of Zhang and Behrens (2000) and write the diffusivity as

$$D \approx D_\infty \exp\left[-\frac{Q}{RT} + \left(-A + \frac{Q_c}{RT}\right)\frac{C}{B}\right] \tag{5}$$

where the prefactor $D_\infty \approx 1.3 \times 10^{-6}\mathrm{m}^2/\mathrm{s}$, the activation energy $Q \approx 109\mathrm{kJ/mol}$, and the gas constant $R = 8.314\mathrm{J/(mol\,K)}$, while the dependence on water concentration C is controlled by the parameters $A \approx 27.2$, $Q_c \approx 307\,\mathrm{kJ/mol}$, and $B \approx 57.14\mathrm{wt.\%}$. The solid line in Fig. 6 shows an estimate of the time required to completely hydrate glass particles of nominal radius $a = 1\,\mathrm{mm}$, with D evaluated for $C = C_{\mathrm{init}} = 0.1\mathrm{wt.\%}$. Hydration rinds of lesser thickness are anticipated when insufficient time is available for transport throughout the glass particles. The hydration time can be reduced significantly when water is able to access the glass interior along fractures that form in part as a result of the stresses induced by changes in temperature and water content. To account approximately for this effect, the dashed line in Fig. 6 shows the diffusion time across spheres of radius $a_{\mathrm{eff}} = 0.1\,\mathrm{mm}$. Notably, the time scale over which the center of the tephra deposit cools significantly for the thermal scenario discussed above (see Fig. 5) is longer than the hydration time (~3 years) for particles of radius $a_{\mathrm{eff}} = 0.1\,\mathrm{mm}$ at an emplacement temperature of 240°C, but much shorter than the hydration time (~300 years) for particles of radius $a = 1\,\mathrm{mm}$.

To further illustrate the expected hydration behavior, consider the idealized case of spherical glass particles with radius a. The equation governing diffusive exchange of water as a function of radius r and time t can be written as

$$\frac{\partial C}{\partial t} = \frac{1}{r^2}\frac{\partial}{\partial r}\left(Dr^2\frac{\partial C}{\partial r}\right), \tag{6}$$

where the concentration at the outer boundary is $C(r = a) = C_{\mathrm{sat}}(t)$ from Eq. (4), symmetry requires that $\partial C/\partial r = 0$ at $r = 0$, and the initial water concentration is set to $C(t = 0) = 0.1\mathrm{wt.\%}$. For our application, D is expected to vary in time due to temperature changes, but its variation in space due to thermal effects is insignificant because the rate of thermal diffusion is so much faster than the rate of compositional diffusion. Instead, spatial variations in D are attributed solely to the effects of the hydration itself on the diffusivity, as described by the C dependence in Eq. (5) – for intuition, at 240°C $D(C_{\mathrm{sat}} \approx 1.52\mathrm{wt.\%}) \approx 3D(C_{\mathrm{init}} = 0.1\mathrm{wt.\%})$. As detailed in the Appendix, we solve Eq. (6) using the Matlab stiff ode integrators to calculate the evolution of C at a prescribed set of equally spaced radial nodes.

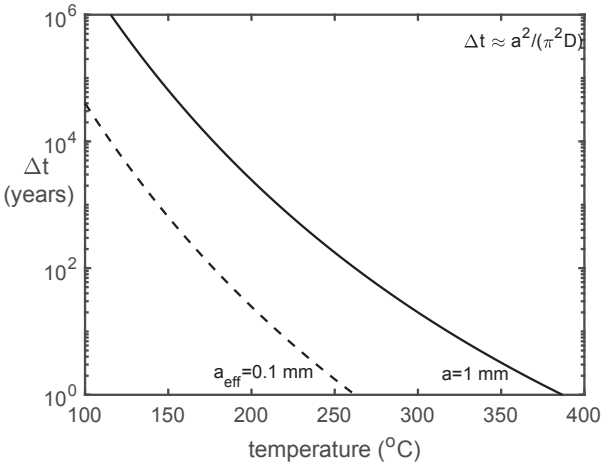

Fig. 6. Temperature dependence of the time required to hydrate glass particles of radius $a = 1\,\mathrm{mm}$ (solid) and $a_{\mathrm{eff}} = 0.1\,\mathrm{mm}$ (dashed) with the compositional diffusivity approximated by Eq. (5) using the nominal parameters from Table 2. The time scale Δt increases with the square of particle radius a, and is inversely proportional to the temperature and hydration dependent diffusivity D.

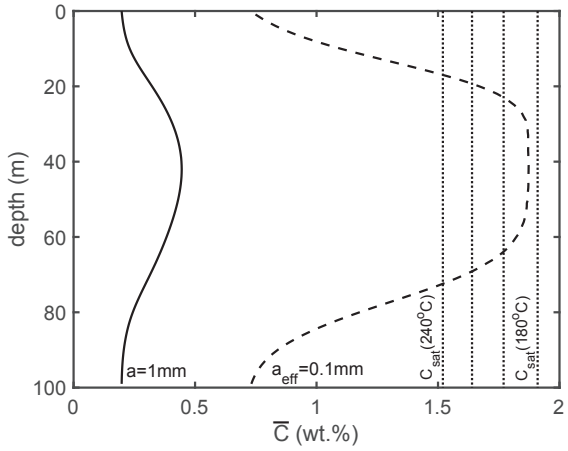

Fig. 7. Average water content $\bar{C}(t) = \left(3\int_0^a r^2 C(r,t)\,\mathrm{d}r\right)/a^3$ in glass particles of radius $a = 1\,\mathrm{mm}$ (solid) and $a_{\mathrm{eff}} = 0.1\,\mathrm{mm}$ (dashed) plotted as a function of depth following the thermal scenario of Fig. 5 with the compositional diffusivity approximated by Eq. (5), the surface concentration given by Eq. (4), and interior concentrations satisfying Eq. (6), calculated using the nominal parameters in Table 2. For reference, the water solubility from Eq. (4) at the emplacement temperature and 20°C cooler increments are indicated by the vertical dotted lines.

Fig. 7 shows the predicted average water content as a function of depth following the hydration of glass particles with the temperature history depicted in Fig. 5. Rapid cooling near the upper and lower boundaries limits compositional transport in these regions, but the interior portion of the tephra layer is held at elevated temperatures for sufficiently long time periods that the average water content in glass particles is expected to increase significantly. For reference, the surface concentration of glass particles (1.52 wt.%) at the emplacement temperature is indicated by the leftmost vertical dotted line. For 0.1 mm particles near the deposit center the average water concentration exceeds this level and more closely matches the concentration in equilibrium with water dissolved at 180°C, whereas the 1 mm particles take up much less water on average. This behavior is further illuminated by examining changes in the average water content through time and profiles of water concentration as a function of distance into particle interiors, which are shown at several representative depths in Fig. 8. The elevated surface water concentrations shown in Fig. 8b) are indicative of cooler temperatures; they cause the average water content of the 0.1 mm spherical particles to exceed the solubility at the emplacement temperature, while the average water content of the 1 mm particles remains lower since a hydrated rind of less than 200 μm thickness is able to form before the temperature cools sufficiently that subsequent diffusion is inconsequential.

2.3. Isotopic evolution

Water that accumulates from precipitation during glacial times is depleted in heavy isotopes in comparison with that which is

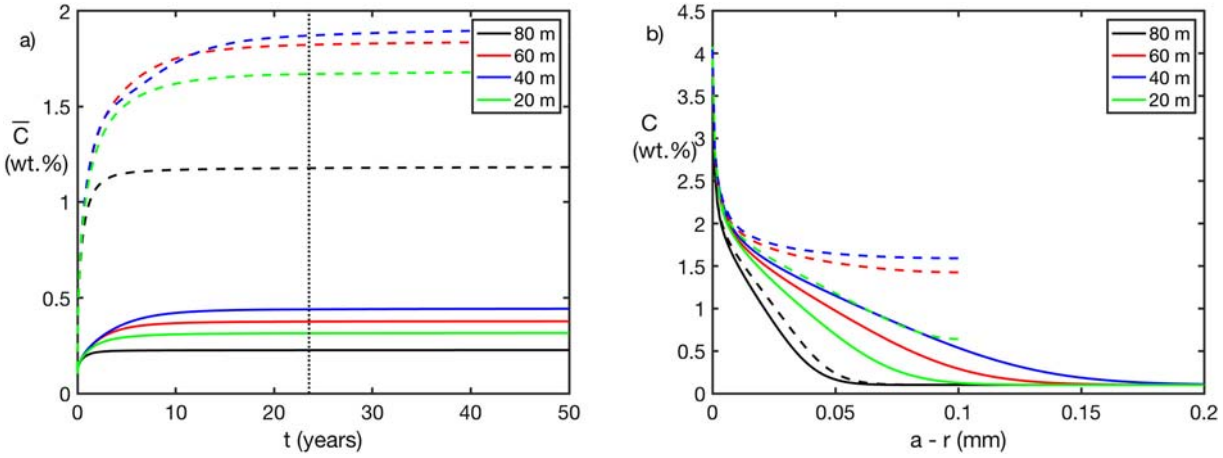

Fig. 8. Hydration of glass through time and space for spherical glass particles of radius $a = 1$ mm (solid) and $a_{\text{eff}} = 0.1$ mm (dashed). a) Average water content $\bar{C}(t) = \left(3\int_0^a r^2 C(r,t)\,dr\right)/a^3$ as a function of time at the depths noted in the legend. The average dissolved water content changes little once the tephra deposit is completely water saturated, as indicated beyond the vertical dotted lined at approximately 24 years. b) Water content as a function of distance from the surface of spherical glass particles following the nominal hydration scenario depicted in Figs. 5 and 7. The increase of diffusivity with water concentration leads to more marked gradients near particle rims than would otherwise be expected.

emplaced during interglacial times. Temperature-dependent fractionation is expected to take place as water enters tephra particles, thereby modifying δD, δ^{18}O and δ^{17}O and causing them to deviate from a meteoric water signature. Following the arguments presented in the Appendix, we describe the fractionation of oxygen and hydrogen isotopes using

$$1000\ln\alpha_{\text{glass-water},^{18}\text{O}} = 3.97\left(\frac{1000\text{ K}}{T}\right)^2 - 4.9\frac{1000\text{ K}}{T} \tag{7}$$

$$1000\ln\alpha_{\text{glass-water},^{17}\text{O}} = 1000\ln\alpha_{\text{glass-water},^{18}\text{O}}\left(0.5305 - \frac{1.85\text{ K}}{T}\right) \tag{8}$$

$$1000\ln\alpha_{\text{glass-water,D}} = -3.15\left(\frac{1000\text{ K}}{T}\right)^2 + 6.12. \tag{9}$$

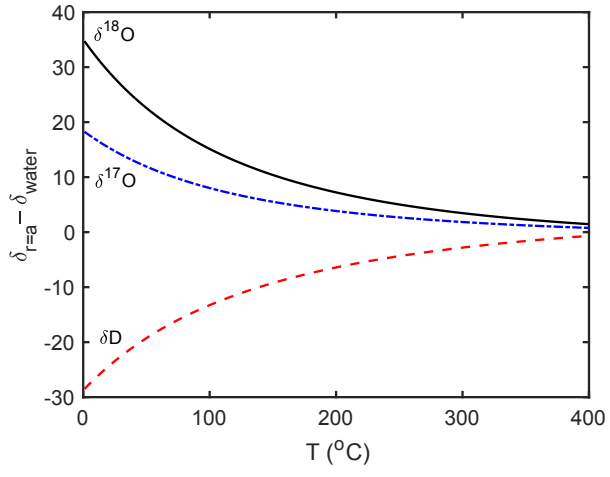

Fig. 9. Temperature dependence of change in isotopic content (in ‰) caused by fractionation at the glass–water interface, from Eqs. (7)–(10). The lowest curve shows the change in δD from a nominal value of $\delta\text{D}_{\text{water}} = -190$‰; the middle and upper curves show the change in δ^{17}O and δ^{18}O from nominal values of $\delta^{17}\text{O}_{\text{water}} = -13$‰ and $\delta^{18}\text{O}_{\text{water}} = -25$‰. Fractionation is most significant at lower temperatures, but decreases with T so that the isotopic content of water dissolved when the deposit is nearest the emplacement temperature is closest to that of the hydrating source.

The concentrations of the heavy isotopes of oxygen and hydrogen at glass surfaces are thereby related to their concentrations $\delta^{18}\text{O}_{\text{water}}$, $\delta^{17}\text{O}_{\text{water}}$ and $\delta\text{D}_{\text{water}}$ in the adjacent pores by

$$\delta i\big|_{r=a} = \alpha_{\text{glass-water},i}\,(1000‰ + \delta i_{\text{water}}) - 1000‰, \tag{10}$$

where the index i is taken to represent ^{18}O, ^{17}O or D. Fig. 9 illustrates the changes in surficial isotopic content as a function of temperature from water with a representative glacial signature. The oxygen isotopic values within the glass are appreciably heavier than the source water, particularly at cooler temperatures, but the hydrogen isotopic

Table 2
Nominal parameter values used to approximate the compositional evolution of hydrating tephra particles. The nominal initial tephra temperature of 240 °C is used to illustrate values for several derived quantities in the lower part of the table (using the listed equation numbers).

Parameter (units)	Nominal value
Diffusion parameter D_∞ (m^2/s) – Eq. (5)	1.3×10^{-6}
Activation energy Q (kJ/mol) – Eq. (5)	109
Gas constant R (J K^{-1} mol^{-1})	8.314
Diffusion parameter A – Eq. (5)	27.2
Diffusion parameter Q_c (kJ/mol) – Eq. (5)	307
Diffusion parameter B (wt.%) – Eq. (5)	57.14
Glass particle radius a (m)	10^{-3}
Fractured effective radius a_{eff} (m)	10^{-4}
Oxygen mass fraction in glass X_O	0.5
Initial water concentration C_{init} (wt.%)	0.1
Glacial meteoric isotopic ratio $\delta^{18}\text{O}_{\text{water}}$ (‰)	−25.000
Glacial meteoric isotopic ratio $\delta^{17}\text{O}_{\text{water}}$ (‰)	−13.246
Glacial meteoric isotopic ratio $\delta\text{D}_{\text{water}}$ (‰)	−190
Magmatic isotopic ratio $\delta^{18}\text{O}_{\text{water}}$ (‰)	7.000
Magmatic isotopic ratio $\delta^{17}\text{O}_{\text{water}}$ (‰)	3.729
Magmatic isotopic ratio $\delta\text{D}_{\text{water}}$ (‰)	−100
Diffusivity $D(T = 240°\text{C}, C = 0.1$ wt.%) (m^2/s) – Eq. (5)	1.1×10^{-17}
Solubility $C_{\text{sat}}(T = 240°\text{C})$ (wt.%) – Eq. (4)	1.52
Fractionation factor $\alpha_{\text{glass-water},^{18}\text{O}}(T = 240°\text{C})$ – Eq. (7)	1.0055
Fractionation factor $\alpha_{\text{glass-water},^{17}\text{O}}(T = 240°\text{C})$ – Eq. (8)	1.0029
Fractionation factor $\alpha_{\text{glass-water,D}}(T = 240°\text{C})$ – Eq. (9)	0.9942
Surface isotopic ratio $\delta^{18}\text{O}_0(T = 240°\text{C})$ (‰) – Eq. (10)	−19.596
Surface isotopic ratio $\delta^{17}\text{O}_0(T = 240°\text{C})$ (‰) – Eq. (10)	−10.368
Surface isotopic ratio $\delta\text{D}_0(T = 240°\text{C})$ (‰) – Eq. (10)	−194.719

value of the glass is shifted to lighter values, as prescribed by the sense of the 1000 ln α fractionations in Eqs. (7)–(9).

Upon emplacement, the small amounts of water contained within the glass particles are expected to be characterized by magmatic isotopic signatures (e.g. $\delta^{18}O \approx 7‰, \delta^{17}O \approx 3.7‰, \delta D \approx -100‰$, see Table 2). Changes in the product $C\delta$ during hydration are driven by diffusive exchange similar to that described by Eq. (6), with δ values at the surface of each particle set to satisfy the glass–water isotope fractionation Eq. (10).

The treatment described in the Appendix also accounts for important complications that result from: 1. the rapid diffusion of hydrogen isotopes by proton exchange that is expected between dissolved water molecules, and 2. the exchange of oxygen isotopes between silica molecules and water molecules dissolved in the glass.

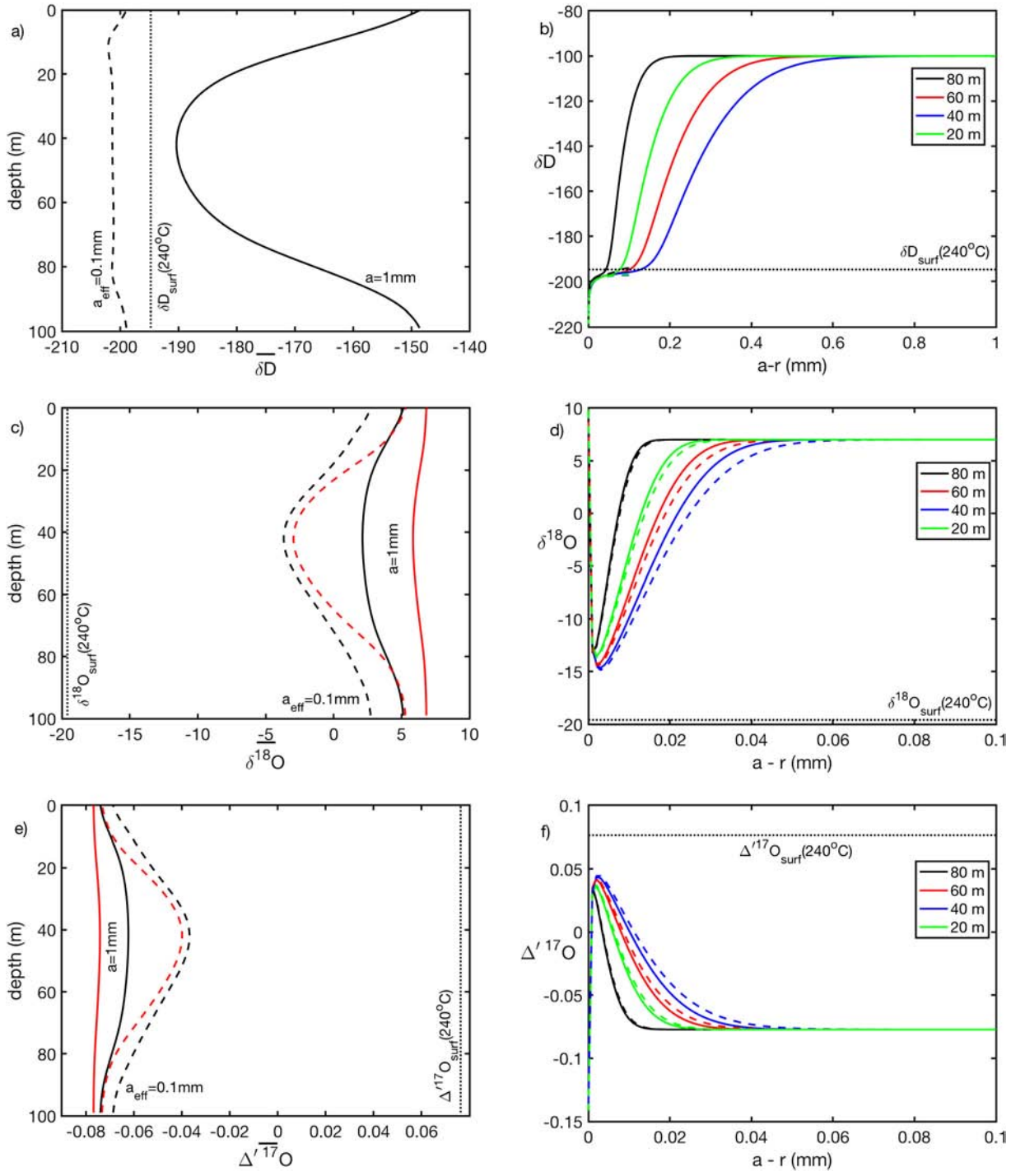

Fig. 10. Isotopic profiles following the nominal hydration scenario depicted in Figs. 5 and 7 calculated for spherical glass particles of radius $a = 1$ mm (solid) and $a = 0.1$ mm (dashed) using the nominal parameters given in Table 2, assuming efficient oxygen exchange between dissolved water and silica. Surface isotopic values fractionated at the emplacement temperature are shown with dotted lines. Left: Radially averaged isotopic content as a function of depth; oxygen isotopic contents of dissolved water are in black, while corresponding bulk glass values are in red. Right: Profiles showing radial changes in the isotopic content of dissolved water within individual particles at the indicated depths. a) & b) δD; c) & d) δ^{18}O; e) & f) Δ'^{17}O.

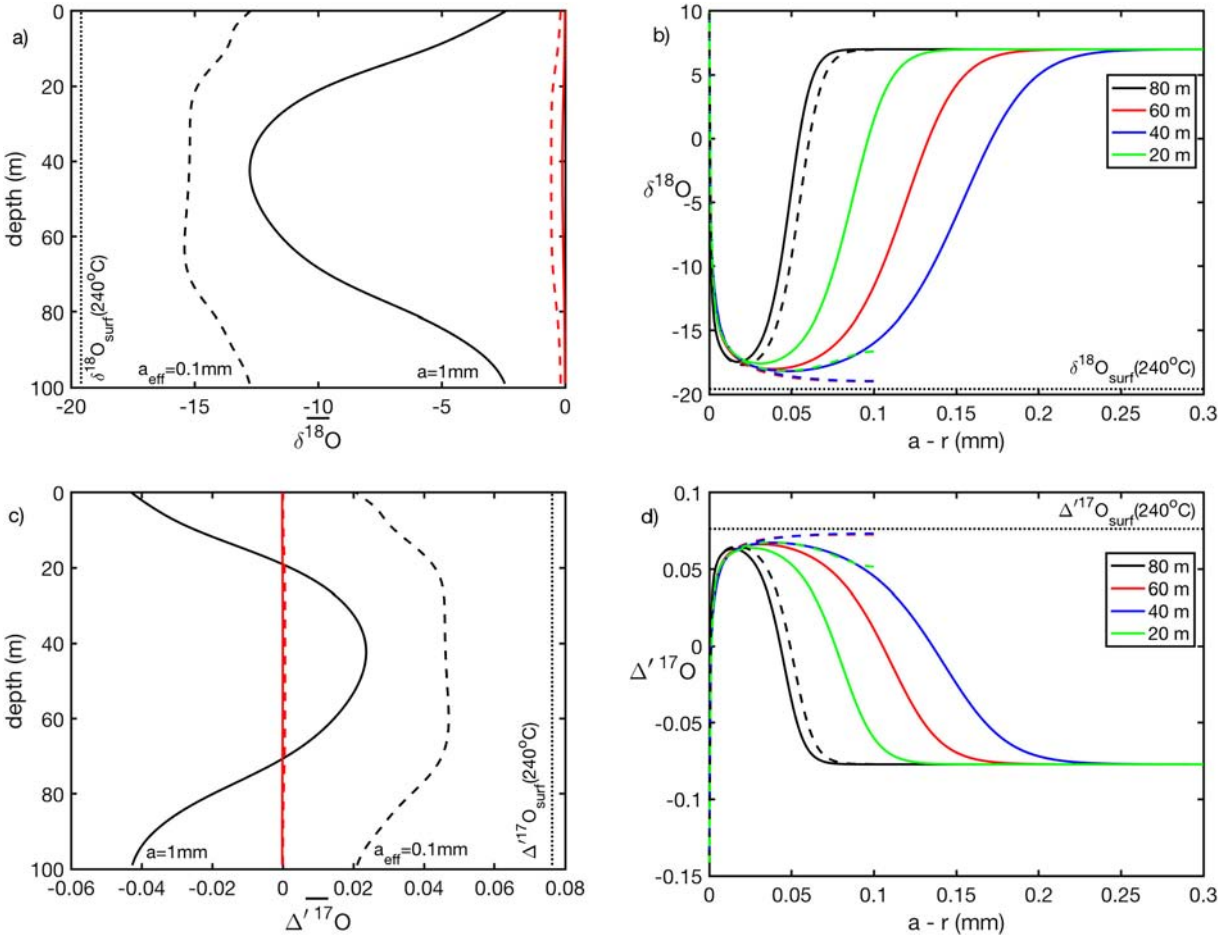

Fig. 11. Isotopic profiles following the nominal hydration scenario depicted in Figs. 5 and 7 calculated for spherical glass particles of radius $a = 1$ mm (solid) and $a = 0.1$ mm (dashed) using the nominal parameters given in Table 2, assuming no oxygen exchange between dissolved water and silica. Left: Radially averaged isotopic content as a function of depth; oxygen isotopic contents of dissolved water are in black, while corresponding bulk glass values are in red. Right: Profiles showing radial changes in the isotopic content of dissolved water within individual particles at the indicated depths. a) & b) δ^{18}O. c) & d) Δ'^{17}O.

Following the solution procedure outlined in the Appendix, Figs. 10 and 11 show the predicted average isotopic content as a function of depth within the tephra deposit, alongside the predicted isotopic profiles within individual particles at a series of depths. In Fig. 10, the oxygen profiles are obtained in the limit that isotopic exchange between dissolved water and silica is rapid, which results in significant retardation to the rate of modification of δ^{18}O and Δ'^{17}O signatures by pore waters (here, $\Delta'^{17}O = \delta'^{17}O - 0.5305\ \delta'^{18}O$ where $\delta'^{17,18}O = 1000\ \ln(1 + \delta^{17,18}O/1000)$ e.g. Bindeman et al. (2018); note the expanded radial scales of Fig. 10d) and f) in comparison with Fig. 10b)). Fig. 11 shows oxygen isotopic profiles in the limiting case where exchange between dissolved water and silica is negligible so that the isotopic signal of meteoric oxygen extends much further from exterior glass surfaces. Isotopic values reflecting the initial magmatic composition are retained at the most shallow tephra depths and near the ice boundary because rapid cooling precludes significant hydration in these regions, whereas glass particles in the interior portion of the tephra layer take up enough fractionated meteoric water to be imparted with a recognizable climatic signature (e.g. low δD values). This is most evident for the δD signal, with average values approaching those of fractionated meteoric water at the emplacement temperature, which are close to that of the original hydrating water. Transport of oxygen isotopes is more gradual because of interactions with silica oxygen; this is especially true for bulk oxygen isotopic compositions (red) whereas water-in-glass values (black) are closer to those of the hydrating water. Radial profiles of isotopic content in mm-scale particles (solid) retain the original magmatic signatures near their centers, with perturbations concentrated in rims that are largest at the mid-tephra depths where high temperatures persist longer. Distant from the comparatively rapid cooling near the upper and lower tephra boundaries, the isotopic signatures of finer particles (dashed) can become completely overwritten by interactions with meteoric water.

3. Results and discussion

To evaluate the potential for inferring past climatic conditions from careful analysis of hydrated tephra deposits, we have focussed upon an idealized physical scenario that is amenable to a simplified model treatment. Although diverse natural volcanic systems will invariably be subject to additional physical complications beyond those considered here, we anticipate that the essential elements addressed by our model should nevertheless yield predictions that are instructive for building intuition and can inform the interpretation of volcanic deposits with a range of post-emplacement histories. With this in mind, in Section 3.1 we discuss the implications of our analysis for the conditions under which volcanic deposits are likely to record evidence of early post-eruptive interactions with melting ice. In Section 3.2 we examine further how isotopic signatures recorded within glass particles might be used to infer characteristics of the syn-eruptive climate. Section 3.3 briefly summarizes some of the broader geological implications of our work.

3.1. Volcanic deposition on ice: tephra and lavas

The time that a volcanic deposit spends at elevated temperatures with access to water is crucial for determining whether or not tephra particles can be hydrated and record meaningful evidence of the syn-eruptive climatic state. The particular physical scenario that we focus upon here, with an inter-caldera deposit covering a thick layer of glacial ice, ensures both an abundant water source and sufficiently gradual cooling that glass particles can hydrate enough to enable such inferences to take place. The broad agreement of the scaling analyses depicted in Figs. 3 and 4 with the modeled thermal evolution shown in Fig. 5 reinforces the expectation that the interior regions of tephra deposits can remain close to the emplacement temperature for several decades, and that the heat extracted to cool a tephra deposit is typically lower than that required to melt an equal thickness of ice. This analysis also supports the intuition that ice can survive inside a buried caldera for many decades and even centuries.

Extending beyond the specific scenario that we have examined, the physical conditions that control hydration are expected to be similar for vesicular lava flows that advance rapidly over an ice cap. For example, the large (50–70 km^3) rhyolitic lavas of Yellowstone likely emanated from elongated fissures with high discharge rates and must have remained active for months to years (Loewen et al., 2017) to keep them from stalling and forming separate lobes. Because of density considerations, rhyolites are expected more typically to erupt *beneath* ice, but the geological evidence from the West Yellowstone flow, particularly the nearly vertical flow wall and numerous tuyas, suggests that this lava pushed up against ice of several hundred meters thickness (Christiansen et al., 2007; Vazquez et al., 2017). One can envision a scenario in which caldera floor topography causes lava to flow over an ice layer, resulting in a geometrical arrangement similar to that examined here for tephras. Notable differences between the burying of ice by tuffs versus lavas include: 1) the hotter interiors of lava flows (ca 800–850 °C as compared with air-cooled tephra temperatures that are generally <600 °C and more typically <400 °C), 2) the comparatively lower permeability of lava immediately following emplacement (i.e. prior to extensive cracking), which may limit water availability, and 3) a broader range of water transport pathways, with the reduced horizontal extents of lava flows potentially leading to enhanced lateral water escape (e.g. Gudmundsson et al., 1997; Squyres et al., 1987). These complications are expected to cause the detailed thermal history to differ, perhaps substantially, from that considered here, with increases to the cooling time helping to foster increased hydration, but the reduction in water solubility at high temperatures and potential reductions in water supply to the pore space having the opposite effect. We note that abundant evidence for lava flows and tephra forming insulating layers at the interface with ice has also been found (e.g. Barr et al., 2018; Edwards et al., 2014, 2012, 2013).

Tephra thicknesses approaching and exceeding 100 m are observed in several Alaskan volcanic centers (e.g. Griggs, 1922; Hildreth and Fierstein, 2012; Miller and Smith, 1987) and other locations that may have been ice-covered at the time of emplacement (e.g. Sheridan, 1970; Scott and Tanaka, 1982). However, it is important to acknowledge the difficulty in finding an intact and exposed field outcrop, let alone an entire cross section, that preserves the hydration features and isotopic profiles described in this work (although the possibility may be enhanced through evidence collected in bore holes). Long after burial when the ice is melted, and perhaps earlier during differential sagging of adjacent portions of cooling tuff units, a mixture of jumbled layers is expected to commonly occur. Such an outcrop might be expected to look like the present day Nez Perce subglacial or subaqueous lava of Yellowstone (its detailed eruption history is not presently known), with perlitic rubble, pillows, dike-like protrusions, and wavy undulations of layering (Christiansen et al., 2007). We suggest that analyzing individual hydrated spheres for oxygen and hydrogen isotopes could serve as a tool for recognizing the processes described by our model, with each sphere representing the thermal and compositional history at a particular location within the deposit. The isotopic signatures predicted by our model are considered in more detail next.

3.2. Isotopic signatures of hydrated tephra

Fig. 12 shows the average isotopic content implied by the nominal thermal scenario for particles with effective radii of 0.1 mm and 1.0 mm hydrated by water with either a glacial climate signature or an interglacial climate signature. Compositional values are plotted for each meter of tephra depth along the entire section. Beginning from the initial magmatic isotopic signature indicated by the labeled green squares, the isotopic content evolves towards that of the fractionated hydrating water, with the closest approach taking place for the smallest particles near the deposit center. Although the temperature dependence of fractionation (see Fig. 9) ensures that glass surfaces in the cooling tephra are subject to a changing isotopic history, the thermal sensitivity of compositional diffusivity (i.e. the

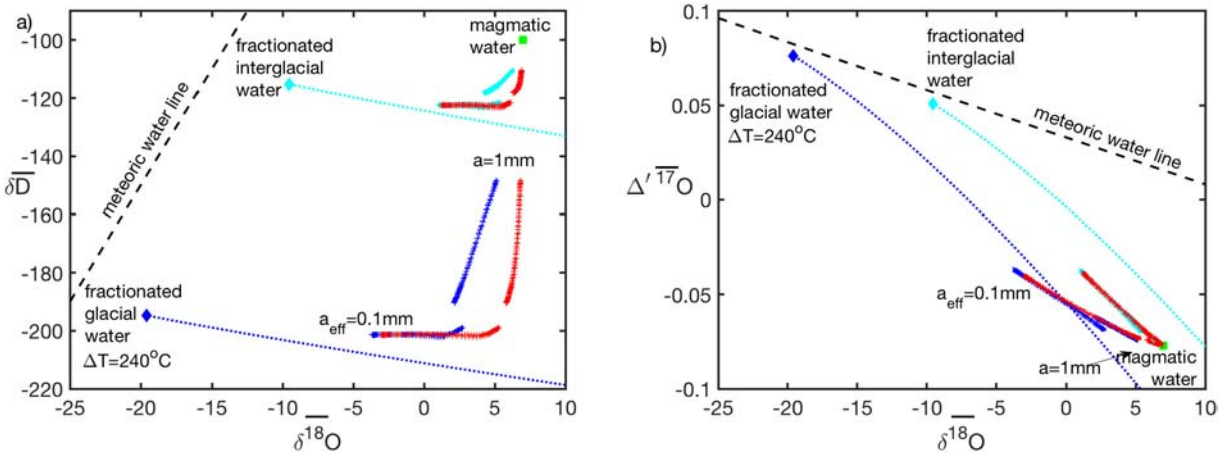

Fig. 12. Average isotopic content throughout the tephra layer following hydration. In each panel the initial magmatic composition is indicated with a green square, the blue dotted line indicates meteoric glacial water fractionated over a temperature range from 0 °C to a peak of 240 °C at the blue diamond, the cyan dotted line terminating in the cyan diamond are for meteoric interglacial water, while the meteoric water line is shown with black dashes. The tephra is deposited at an initial temperature of $\Delta T = 240$°C with 0.1 wt.% magmatic water. a) Average δD vs. δ^{18}O for the labeled particle sizes, with whole-glass isotopic content shown in red and water-in-glass values for hydration with interglacial water shown in cyan and with glacial water shown in blue. b) Average Δ'^{17}O vs. δ^{18}O using the same color scheme as in panel a).

mechanism behind diffusive closure) tends to favor progress towards *isotopic values that characterize the original emplacement temperature*. These are illustrated in Fig. 12 with a dark blue diamond for fractionated hydrating water with a meteoric glacial signature and with a cyan diamond for the interglacial case. Because the transport of hydrogen isotopes is much more rapid than the transport of oxygen isotopes, Fig. 12a) shows that δD values approach equilibrium with the hydrating water throughout most of the deposit for the 0.1 mm particles, and even in portions of the deposit with 1 mm particles, whereas the $\delta^{18}O$ values remain much closer to the original magmatic composition. In this particular modeling scenario, we assume efficient exchange of oxygen isotopes between dissolved water and silica, with the result that the whole glass averages of oxygen isotopic content (red) are even closer to the magmatic initial values than the averages of the water-in-glass component (blue: glacial, cyan: interglacial). The variations of $\Delta'^{17}O$ with $\delta^{18}O$ shown in Fig. 12b) for water-in-glass and whole-glass averages follow similar trends that approach a linear mixing line between the isotopic compositions of the initial magmatic and fractionated hydrating water.

Further calculations indicate general trends in behavior such that alternative parameter choices that favor longer time frames at elevated temperatures (e.g. larger tephra thickness H_t, higher porosity n) cause the isotopic contents of glass particles to more closely resemble those of the fractionated hydrating water. Because changes to the deuterium content are much more rapid than changes to the oxygen isotopic content, plots of δD against $\delta^{18}O$ tend to run almost parallel to the trend of meteoric water fractionated at different temperatures (i.e. the dotted lines in Fig. 12). Similarly, measurements of $\Delta'^{17}O$ against $\delta^{18}O$ are also expected to approximately follow fractionated meteoric trends, as shown in Fig. 12b). These observations suggest that isotopic data from hydrated glass particles in rapidly changing thermal regimes are unlikely to yield good constraints on emplacement temperature, but may record isotopic closure temperatures in their hydrated rims. However, the total water content does give a reasonable indication of the solubility at temperatures near those of tephra emplacement; as discussed above, this is particularly true for measurements on the entirety of smaller particles and spot measurements from the interiors of larger particles. With measurements of isotopic content at multiple tephra depths, extrapolation of the trends in oxygen isotopic data can give a reasonable estimate for the isotopic signature of the fractionated meteoric water, as illustrated by the data plotted in Fig. 12, and in recent detailed observations of Mount Mazama's pinnacles (Hudak and Bindeman, 2018).

It is worth again drawing attention to the significant uncertainties that remain in the dependence of diffusivity on temperature and water content, as well as the detailed nature of interactions between the oxygen of dissolved water and silica. Our calculations suggest that more rapid diffusive transport is likely to cause measurements of glass isotopic content to more closely mimic those of the hydrating water, but the essential trends that we obtain using the nominal parameter values appear to be robust. Even without accounting for the rapid self-diffusion of hydrogen in dissolved water, deuterium signatures evolve much more rapidly than oxygen isotopic values simply because of the large oxygen stores that are held within the silica of glass.

To keep the treatment simple, we have neglected any tendency for the isotopic content of the hydrating water to evolve. In our application we are justified in ignoring potential "reservoir effects" because the rate at which water is incorporated into glass is much slower than the rate at which water transits through the pore space. In fact, a scaling argument outlined in the Appendix suggests that on the order of 10^5 water molecules transit the pore space for each water molecule that enters a glass particle.

3.3. Geologic consequences of ice burial during caldera collapses and future directions

The collapse of calderas under ice has not been observed historically and the most promising sites for uncovering evidence of past events are likely limited to glaciated high-latitude volcanically active areas of Kamchatka, Alaska and Iceland, as well as high-altitude glaciated volcanically active areas, such as the Andes. There is a need to further investigate the Pleistocene record in those areas (Fig. 2), and identify the isotopic and other signatures that may betray their presence. As mentioned in the Introduction, subglacial caldera collapses were likely common phenomena during Paleoproterozoic (2.4–2.3 Ga) and Neoproterozoic (0.8–0.6 Ga) pan global Snowball Earth episodes, with estimated glaciation durations extending >10 million years. Although hydrated volcanic glass is unlikely to survive in such ancient deposits, and hydrogen isotopic records are likely compromised, the proposed mechanism that we describe here (Fig. 12) should have left preserved isotopic records in triple oxygen signatures of coeval low-$\delta^{18}O$ rocks, even if these were later metamorphosed. It is thus instructive to examine values of alteration minerals found in tuff beds that developed after alteration by melting ice, as triple oxygen isotopes should be minimally affected.

Furthermore, it is worth taking a broader look at recent and Pleistocene intracaldera tuffs, ignimbrites, and lavas formed over melting ice in models and in nature, to see if they may partially preserve their original structural integrity and simply sag into the ice (Fig. 5), or crumble, structurally-disintegrated into subglacial or postglacial lakes. The historically observed 1996 Gjalp eruption under Vatnajokull in Iceland, characterized by the reverse geometry to our scenario with magma underneath, has caused observable sagging. Gudmundsson et al. (1997) described effects of this subglacial eruption: 3–4 km^3 of glacial meltwater was produced from a modern, warm glacier by a 1100°C basaltic magma, water escaped with temperature of 10–20 °C maintaining ice/magma contact. The basalt formed a 0.75 km^3 hyaloclastitic mound (density of 1.5 –1.6 g/cm^3) at estimated nearly total heat transfer efficiency. Edwards et al. (2015) observed that the snow melted by 4 m in 24 h under the basaltic lava from Tolbachik volcano in Kamchatka.

Geologic evidence of ice burial in a caldera may be difficult to recognize in the field from often poorly exposed, vegetated, and later uplifted and eroded outcrops. Thick layers of ice may cool overlying tephra before complete melting and disappearance. As an example, a meter thick, cooled tephra layer still covers pre-1912 CE ice in Katmai National Park today (Hildreth and Fierstein, 2012). Upon tephra layer cooling, the subsequent residence of buried ice in calderas, $10^2 - 10^3$ m below the surface, will melt on geothermal timescales (upper curve in Fig. 5a)). The rates of down movement of the ice–tephra boundary will translate into centimeter per year down-sagging lasting many centuries after caldera collapse, leading to persistent depression of only the overlying tephra layer and not the entire caldera block.

Lastly, we note that extensions to this work are amenable for laboratory study by using transparent container walls and natural hot, dehydrated tephras, or synthetic spherical glass particles, emplaced on large quantities of ice that would melt for long enough durations for hydration to take place, enabling subsequent examination of isotopic variations. Our ongoing lab experiments at 375–175 °C (e.g. Hudak and Bindeman, 2018), and previous hydration experiments at 100 °C (Friedman et al., 1966) suggest that ice surviving for several days should be sufficient. Fig. 13 presents photographs of a "kitchen" experiment in which a 250 °C tephra was put on an initially −10°C block of ice inside of a quartz glass. We observed steaming of the tephra surface and ice melting, leading to the sagging of the ice/tephra boundary. Later in the experiment, regularly spaced hot spots appeared on the upper surface of the tephra, suggesting a fingered regime of water escape similar to that which formed the Crater

Fig. 13. Hot 250 °C basaltic tephra on top of −10 °C ice in a jar. a) Side view, glass is protected by clear tape to prevent breakage. b) Top view showing wetting the surface by escaping steaming fluids. No water layer formation was observed until the tephra cooled completely.

lake pinnacles. Our modeling suggests that hydrogen and oxygen isotope analyses and hydration measurements across such an experimental deposit, should yield measurable signals within several days to weeks of experimental ice melting. For example, measureable isotopic shifts were observed in lava emplaced on ice experiments by Edwards et al. (2013) within hours of interaction.

4. Conclusions

Ice burial inside of calderas is expected to be a common phenomenon in glaciated areas. Although definitive evidence has yet to be recognized from recent Pleistocene glaciations, our analysis suggests that detailed examination of hydrated volcanic products might be used to identify such events, both in the recent past and during more ancient glacial episodes such as the long-lived Snowball Earth events. Our assessment of heat extraction by cooling inter-caldera tephra predicts that glacial ice of moderate thickness (e.g. ≥100 m) should survive as a persistent meltwater source for durations of decades to centuries. To illustrate the hydration of glass particles and the evolution of the associated content of water isotopes, we have considered a nominal tephra deposit thickness of 100 m (similar to observations from large Holocene events, e.g. Griggs, 1922; Hildreth and Fierstein, 2012; Miller and Smith, 1987) and a nominal emplacement temperature of 240 °C that is chosen to be lower than characteristic temperatures for the breakdown of glass to form clays (notably much cooler than typical rhyolitic eruptive temperatures ~ 700–800 °C). Hydration by vapor escaping from the underlying ice source is most effective in the interior of the tephra layer where high temperatures are maintained for longest; we find that 100-micron radius particles become fully saturated to water contents of several weight percent, while significant water uptake in mm-scale particles is limited to an outer rind ~200μm in thickness. Our treatment of isotopic exchange predicts that deuterium signatures within the hydrated glass particles should provide a good indication of the isotopic content of the hydrating water source. The rate at which oxygen isotopic content evolves can be retarded significantly by exchange between dissolved water and the oxygen in the silica molecules of the glass itself. Our results demonstrate nevertheless how the isotopic signatures of hydrated glass particles, alongside their total dissolved water content, can be used both as paleoclimatic indicators and gauges of the tephra emplacement temperature.

Acknowledgments

Partial funding for INB derived from NSF grant EAR1822977.

Appendix A. Model details

It is convenient to divide the processes that determine the $\delta^{18}O$, $\delta^{17}O$ and δD content in altered volcanic glasses (deposited with tephra on ice) into two separate stages. First, we formulate the thermal problem to approximate the variations in temperature through time and space. Second, we formulate the compositional problem to predict the evolving concentrations of stable water isotopes in glass particles contained within the tephra. Descriptions of each of these problems are provided next.

A.1. Thermal problem

Tephra with thickness H_t and porosity n melts its way through ice with thickness $H_i(t)$, with t representing the time since emplacement. Here, we assume the ice is at constant temperature T_m, and the tephra is initially at temperature $T_m + \Delta T$. We take $\Delta T > 100$ °C, which implies that an internal boundary develops between vapor- and liquid-saturated tephra at level $H_v(t)$. The first task is to determine how the temperature profile evolves.

Defining $\bar{\rho C}_{l,v}$ and $k_{l,v}$ as the average volumetric heat capacity and thermal conductivity of the liquid (l) and vapor (v) saturated regions, $\rho_{l,v}C_{l,v}$ as the volumetric heat capacity of the liquid and vapor components, and $u_{l,v}$ as the Darcy velocity for liquid water and vapor, the one-dimensional (z positive upwards) heat flow is described by

$$\bar{\rho C}_l \frac{\partial T}{\partial t} = k_l \frac{\partial^2 T}{\partial z^2} - \rho_l C_l \, u_l \frac{\partial T}{\partial z} \quad \text{for} \quad H_i \le z \le H_v, \tag{A.1}$$

$$\text{and} \quad \bar{\rho C}_v \frac{\partial T}{\partial t} = k_v \frac{\partial^2 T}{\partial z^2} - \rho_v C_v \, u_v \frac{\partial T}{\partial z} \quad \text{for} \quad H_v \le z \le H_i + H_t. \tag{A.2}$$

Treating the vapor phase as an ideal gas implies that $\rho_v C_v = 2P/(5T)$, where P is the vapor pressure and T is temperature. We note that capillary effects may conspire to produce a mixed region with partial saturation of the tephra pore space by coexisting liquid and vapor. To focus on the most essential elements of the problem we neglect such complications and assume a sharp transition from liquid- to vapor-saturated tephra.

The boundary conditions and liquid Darcy velocity must satisfy i) thermal equilibrium at the ice–tephra boundary, ii) heat balance at the ice–tephra boundary, iii) heat balance at the tephra–atmosphere boundary, and iv) mass balance at the ice–tephra boundary, so that

$$T(H_i, t) = T_m, \tag{A.3}$$

$$\left.\frac{\partial T}{\partial z}\right|_{(H_i)^+} = -\frac{\rho_i L_m}{k_l} \frac{\mathrm{d}H_i}{\mathrm{d}t}, \tag{A.4}$$

$$\left.\frac{\partial T}{\partial z}\right|_{(H_i+H_t)^-} = -\frac{Q_t}{k_v}, \tag{A.5}$$

$$\text{and} \quad u_l(H_i) = (n-1)\frac{\mathrm{d}H_i}{\mathrm{d}t}, \tag{A.6}$$

where $\rho_i L_m$ is the volumetric latent heat of fusion, Q_t is the heat flux at the tephra–atmosphere boundary (discussed further below), and the superscripts $()^{\pm}$ are used to indicate on which side of the boundary (above '+', below '–') the quantity in () is evaluated. In adopting Eq. (A.6), we neglect the potential for fluid loss through ice fractures or lateral flow (such loss would lower the rate of liquid infiltration, thereby increasing the time during which tephra interacts with water vapor at higher temperatures). To further simplify matters we also ignore changes in liquid density and neglect compaction so that u_l is spatially uniform (though time-dependent). In the vapor-saturated region, since vapor density ρ_v is a function of temperature and pressure and so can change significantly, the Darcy velocity satisfies

$$\frac{\partial u_v}{\partial z} = \frac{n}{\rho_v}\frac{\partial \rho_v}{\partial t} - \frac{u_v}{\rho_v}\frac{\partial \rho_v}{\partial z}, \tag{A.7}$$

where the vapor density can be approximated by $\rho_v \approx P/(\tilde{R}T)$, where $\tilde{R}$ is the (mass-based) gas constant. The mass and heat flux conditions at the phase-change boundary give

$$u_v(H_v, t) = \frac{\rho_l}{\rho_v} u_l - \left(\frac{\rho_l}{\rho_v} - 1\right) n \frac{\mathrm{d}H_v}{\mathrm{d}t} \tag{A.8}$$

$$\frac{\mathrm{d}H_v}{\mathrm{d}t} = \frac{u_l}{n} + \frac{k_l}{\rho_l L_v}\left.\frac{\partial T}{\partial z}\right|_{(H_v)^-} - \frac{k_v}{\rho_l L_v}\left.\frac{\partial T}{\partial z}\right|_{(H_v)^+}, \tag{A.9}$$

where $\rho_l L_v$ represents the latent heat of vaporization. Eqs. (A.8) and (A.9) can be combined to write

$$u_v(H_v, t) = u_l - \frac{k_l n}{\rho_v L_v}\left.\frac{\partial T}{\partial z}\right|_{(H_v)^-} + \frac{k_v n}{\rho_v L_v}\left.\frac{\partial T}{\partial z}\right|_{(H_v)^+}. \tag{A.10}$$

The heat flux from the tephra to the atmosphere is attributed primarily to convective and radiative transfer. (An additional contribution can be included to represent the heat loss required to vaporize precipitation, but this is expected typically to be of secondary importance.) The radiative component of heat loss is estimated from

$$Q_r = -\sigma\left(T^4 - T_r^4\right), \tag{A.11}$$

where $\sigma \approx 5.67 \times 10^{-8}\mathrm{W/(m^2\ K^4)}$ is the Stefan–Boltzmann constant and T_r is the radiant temperature along the line of sight from the tephra, which is at temperature T. In detail, we expect T_r to experience both diurnal and annual variations and be influenced by such variables as the degree to which cloud cover obscures the night sky, but on average it should be close to (i.e. deviating by less than 10% from) the local mean annual temperature T_a. We describe convective heat transfer using Newton's law of cooling, which assumes a linear dependence on the temperature difference between the surface and the ambient surroundings so that

$$Q_c = -h\,(T - T_a)\,. \tag{A.12}$$

Here, the heat transfer coefficient h depends on the flow of air (i.e. wind) over the surface and details of the micro-topography; we use a nominal value of $h \approx 20\mathrm{W/(m^2\ K)}$ in our calculations. Together these contributions extract heat from the tephra surface at rate $Q_t \approx Q_r + Q_c$.

To solve for the evolution of temperature as a function of height z within the tephra layer, we discretize the governing Eqs. (A.1) and (A.2) in space and use the stiff ode solvers from Matlab to determine the temperature history at each of the N evenly spaced nodes. The evolving position of the ice–tephra boundary needed to satisfy Eq. (A.1) subject to the equilibrium condition (A.3), the heat flux condition (A.4), and the mass balance condition (A.6) is approximated from

$$\frac{\mathrm{d}H_i}{\mathrm{d}t} \approx \frac{k_l}{(H_t/N)\,\rho_l C_l\,(1-n)}\left[1 - \sqrt{1 + \frac{2\rho_l C_l\,(1-n)}{\rho_i L_m}\,(T_1 - T_m)}\right], \tag{A.13}$$

where $T_1 \equiv T(H_i + H_t/N, t)$. Comparing the magnitudes of the conductive and advective heat transfer terms in Eq. (A.2) and recognizing that $\rho_v C_v u_v (H_i + H_t - H_v)/k_v = 2P u_v (H_i + H_t - H_v)/(5Tk_v) \ll 1$ (i.e. small Peclet number) justifies neglect of advective heat transfer within the vapor-saturated region. This simplifies the treatment by eliminating the need to solve Eq. (A.7) and determine the evolution of vapor transport and pressure within the tephra. For numerical convenience we set the initial temperature within the tephra to $T_m + \Delta T$ everywhere except at the first node above the ice boundary, which we set to the boiling point T_v so that the initial location of H_v is elevated above H_i by the node spacing H_t/N. Combining Eqs. (A.6) and (A.9), subsequent motion of the vaporization front satisfies

$$\frac{\mathrm{d}H_v}{\mathrm{d}t} \approx -\frac{1-n}{n}\frac{\mathrm{d}H_i}{\mathrm{d}t} + \frac{k_l}{\rho_l L_v}\left(\frac{T_v - T_{v^-}}{H_v - H_{v^-}} - \frac{k_v}{k_l}\,\frac{T_{v^+} - T_v}{H_{v^+} - H_v}\right), \tag{A.14}$$

where $H_{v^\pm}$ and $T_{v^\pm}$ refer to the node locations and corresponding temperatures immediately above and below H_v.

Once the temperature at the tephra–atmosphere surface falls below T_v, condensation is expected to enable a second moving boundary to form that marks the location where liquid water occupies the pore space once again, overlying the vapor-saturated region beneath. This should have a warming effect in the region where condensation takes place, and liquid percolation and vaporization are expected to further cool the region just below. Although these effects can be important for modifying the detailed thermal evolution at later times, our calculations demonstrate that changes to the water isotopes contained in tephra particles are not particularly sensitive to the rate of cooling at lower temperatures – essentially because the compositional diffusivities are so much larger at higher temperatures. Accordingly, we ignore this complication to the thermal evolution for the calculations shown here.

A.2. Compositional problem

With the temperature approximated as a function of space and time, determining the influence of water–tephra interactions on the isotopic content of hydrated glass is the next task. Glacial ice is depleted in deuterium and the heavier isotopes of oxygen so that the source water for hydration is at a concentration for each of these species that is much lower than modern values. As water flows through the tephra, glass particles are progressively hydrated and temperature-dependent fractionation processes cause the composition of this water at the particle surfaces to be modified. Because diffusive mass transfer of water into the glass is much slower than the advective water flux through the tephra, the isotopic modification to the glacial melt is unimportant and the isotopic content of the pore water can be treated as constant. Scaling arguments suggest that the ratio of pore water transport to glass uptake can be approximated as $r_{t/u} = \rho_l u_l n/(\rho_{\text{glass}} D\nabla C)$, where $\rho_{\text{glass}} \approx 2.65 \times 10^3$ kg/m^3 is the glass density, we take $\rho_l u_l \sim \rho_v u_v$ as the volumetric Darcy flux, and evaluating $D\nabla C$ at early times while the tephra is hot leads to $r_{t/u} > 10^5$.

Eq. (6) describes the evolution of water content within glass particles that are idealized as spheres of radius a. We insert the evolution of temperature $T(z,t)$ into Eq. (4) to obtain the evolution of the surface water concentration $C_a(t)$ in glass particles that are located at a sequence of depths z. The dependence of the diffusivity D on water concentration C in Eq. (5) complicates the diffusive flux within each particle because it makes D vary along the radial coordinate r. Accordingly we discretize C at equally spaced intervals in r and use the stiff ode integrators in Matlab to solve for the evolution at each node through time while enforcing the zero flux condition at $r = 0$ that is required by symmetry. Simple code verification tests were performed by comparison against the truncated series solution given by Carslaw and Jaeger (1959, p. 233) for the special case where D is treated as spatially uniform, $C(r = a) = C_a(t)$, and $C(t = 0) = f(r)$. Once we have determined $C(r,t)$ at each depth, the spherically averaged water content is approximated using the trapezoid rule as

$$\bar{C}(t) \approx \frac{3}{a^3 N_r}\left(\sum_{i=1}^{N_r} C_i r_i^2 + C_a \frac{a^2}{2}\right), \tag{A.15}$$

where the index i is defined so that C_i is the evolving concentration at $r_i = (i-1)a/N_r$.

Alongside changes in the total water content within glass particles, the hydrogen and oxygen isotopic signatures are also expected to evolve. We assume that surface concentrations deviate from those of the pore constituents according to the temperature dependent fractionation factors given in Eqs. (7)–(9). For δ^{18}O, the polynomial form we use has been shown to characterize fractionation factors for quartz (Sharp et al., 2016) and several common clay minerals (Zheng, 1993; Zheng et al., 1993). Following Bindeman et al. (2018), in Eq. (7) we adopt coefficients that represent weighted fractionations of 70% illite to 30% quartz as approximating the characteristic composition for volcanic glasses. It should be noted that known fractionation factors between different silicate minerals tend to be quite similar so compositional differences between different glasses are not expected to have a substantial effect on the essential behavior that is our focus here. Bindeman et al. (2018) calibrated the fractionation Eq. (8) we use for δ^{17}O, which scales the δ^{18}O fractionation by a factor that rises to 0.5305 at the high-temperature limit (Pack and Herwartz, 2014). Hydrogen fractionation is expected to have the opposite temperature trend to that of the oxygen isotopes. Glass–water fractionation factors have not been measured as a function of temperature, but can be inferred from experiments on micas and empirical observations, particularly from shales. Accordingly, for the calculations shown here we adopt the temperature dependent relationship derived by Hudak and Bindeman (2018).

With the surface isotopic content fixed by Eq. (10) and the relevant temperature-dependent fractionation factors, the isotopic profiles through each spherical particle remain to be determined. For the hydrogen–deuterium case these constituents are wholly associated with the presence of water molecules. Nevertheless, since hydrogen diffusion between water molecules is expected to occur more rapidly than the diffusion of the water molecules themselves, two components to the flux evolution must be accounted for. Denoting the self-diffusivity of hydrogen by D_d, as distinct from the diffusivity of water D, the evolution of the total deuterium content is described by

$$\frac{\partial\,(C\delta D)}{\partial t} = \frac{1}{r^2}\frac{\partial}{\partial r}\left[r^2 D_d \frac{\partial\,(C\delta D)}{\partial r} - r^2\,(D_d - D)\,\delta D \frac{\partial C}{\partial r}\right]. \tag{A.16}$$

For the calculations shown here we assume a nominal value of $D_d = 10D$. We adopt a spatial discretization procedure analogous to that described above for the total water content to track the evolution of deuterium content at a sequence of radial nodes and approximate the spherically averaged deuterium content using the trapezoid rule.

The evolution of oxygen isotopic content may be complicated by exchange between dissolved water and the oxygen within glass molecules. We expect this exchange to maintain the ratio of the concentrations of ^{18}O and ^{17}O in glass molecules to those in the dissolved water near values of Γ_{18} and $\Gamma_{17} \approx (\Gamma_{18})^{\theta}$ respectively, where (Sharp et al., 2016)

$$\theta \approx -\frac{1.85 \pm 0.04\ \text{K}}{T} + 0.5305. \tag{A.17}$$

Without firm constraints on intra-glass water–silicate fractionation, we explore two limiting cases. To examine the case where exchange of oxygen between dissolved water and silica is rapid, we perform a set of calculations with $\Gamma_{18} = \Gamma_{17} = 1$. To examine the opposite case where negligible exchange of oxygen takes place between the dissolved water and silica, we perform a set of calculations with $\Gamma_{18} = \Gamma_{17} = 0$. We take the oxygen mass fraction in rhyolitic glass to be $X_O \approx 0.5$ for the typical compositions encountered. Denoting the self-diffusivity of oxygen in glass by D_O, these considerations suggest that the isotopic content evolves as

$$\frac{\partial}{\partial t}\left(C\delta^{18}\text{O} + X_O\Gamma_{18}\delta^{18}\text{O}\right) = \frac{1}{r^2}\frac{\partial}{\partial r}\left[r^2 D\frac{\partial\,(C\delta^{18}\text{O})}{\partial r} + r^2 D_O X_O \Gamma_{18}\frac{\partial \delta^{18}\text{O}}{\partial r}\right], \tag{A.18}$$

with an analogous expression governing the evolution of $\delta^{17}O$. Because silica to silica diffusion of oxygen molecules is expected to be very slow at operative temperatures (i.e. $<400\,^{\circ}$C), we anticipate that $D \gg D_O$ justifying neglect of the second term in brackets on the right.

References

Anovitz, L.M., Cole, D.R., Fayek, M., 2008. Mechanisms of rhyolitic glass hydration below the glass transition. Am. Mineral. 93 (7), 1166–1178.

Anovitz, L.M., Elam, J.M., Riciputi, L.R., Cole, D.R., 1999. The failure of obsidian hydration dating: sources, implications, and new directions. J. Archaeol. Sci. 26 (7), 735–752.

Anovitz, L.M., Elam, J.M., Riciputi, L.R., Cole, D.R., 2004. Isothermal time-series determination of the rate of diffusion of water in Pachuca obsidian. Archaeometry 46 (2), 301–326.

Bacon, C.R., 1983. Eruptive history of Mount Mazama and Crater Lake caldera, Cascade Range, USA. J. Volcanol. Geotherm. Res. 18 (1-4), 57–115.
Barr, I.D., Clark, C.D., 2012. Late Quaternary glaciations in far NE Russia: combining moraines, topography and chronology to assess regional and global glaciation synchrony. Quat. Sci. Rev. 53, 72–87.
Barr, I.D., Lynch, C.M., Mullan, D., De Siena, L., Spagnolo, M., 2018. Volcanic impacts on modern glaciers: A global synthesis. Earth Sci. Rev. 182, 186–203.
Bigg, G., Clark, C., Hughes, A., 2008. A last glacial ice sheet on the Pacific Russian coast and catastrophic change arising from coupled ice-volcanic interaction. Earth. Planet. Sci. Lett. 265 (3), 559–570.
Bindeman, I., Leonov, V., Izbekov, P., Ponomareva, V., Watts, K., Shipley, N., Perepelov, A., Bazanova, L., Jicha, B., Singer, B., et al. 2010. Large-volume silicic volcanism in Kamchatka: Ar-Ar and U-Pb ages, isotopic, and geochemical characteristics of major pre-Holocene caldera-forming eruptions. J. Volcanol. Geotherm. Res. 189 (1), 57–80.
Bindeman, I., Zakharov, D., Palandri, J., Greber, N.D., Dauphas, N., Retallack, G., Hofmann, A., Lackey, J., Bekker, A., 2018. Rapid emergence of subaerial landmasses and onset of a modern hydrologic cycle 2.5 billion years ago. Nature 557 (7706), 545.
Bindeman, I.N., Lowenstern, J.B., 2016. Low-δD hydration rinds in Yellowstone perlites record rapid syneruptive hydration during glacial and interglacial conditions. Contrib. Mineral. Petrol. 171 (11), 89.
Carslaw, H., Jaeger, J., 1959. Heat in Solids. vol. 1. Clarendon Press, Oxford.
Christiansen, R.L., Lowenstern, J.B., Smith, R.B., Heasler, H., Morgan, L.A., Nathenson, M., Mastin, L.G., Muffler, L., Robinson, J.E., 2007. Preliminary assessment of volcanic and hydrothermal hazards in Yellowstone National Park and vicinity. Tech. rep.. U. S. Geological Survey.,
Crowley, J., Schoene, B., Bowring, S., 2007. U-Pb dating of zircon in the Bishop Tuff at the millennial scale. Geology 35 (12), 1123–1126.
Dansgaard, W., Johnsen, S., Clausen, H., Dahl-Jensen, D., Gundestrup, N., Hammer, C., Hvidberg, C., Steffensen, J., Sveinbjörnsdottir, A., Jouzel, J., et al. 1993. Evidence for general instability of past climate from a 250-kyr ice-core record. Nature 364 (6434), 218–220.
Dean, W.E., Kennett, J.P., Behl, R.J., Nicholson, C., Sorlien, C.C., 2015. Abrupt termination of marine isotope stage 16 (termination VII) at 631.5 ka in Santa Barbara Basin, California. Paleoceanography 30 (10), 1373–1390.
Duan, X., 2014. A general model for predicting the solubility behavior of H_2O-CO_2 fluids in silicate melts over a wide range of pressure, temperature and compositions. Geochim. Cosmochim. Acta 125, 582–609.
Edwards, B., Belousov, A., Belousova, M., 2014. Propagation style controls lava-snow interactions. Nat. Commun. 5, 5666.
Edwards, B., Magnússon, E., Thordarson, T., Gudmundsson, M., Höskuldsson, A., Oddsson, B., Haklar, J., 2012. Interactions between lava and snow/ice during the 2010 Fimmvörduháls eruption, south-central Iceland. J. Geophys. Res. Solid Earth 117 (B4).
Edwards, B.R., Belousov, A., Belousova, M., Melnikov, D., 2015. Observations on lava, snowpack and their interactions during the 2012–13 Tolbachik eruption, Klyuchevskoy Group, Kamchatka, Russia. J. Volcanol. Geotherm. Res. 307, 107–119.
Edwards, B.R., Karson, J., Wysocki, R., Lev, E., Bindeman, I., Kueppers, U., 2013. Insights on lava-ice/snow interactions from large-scale basaltic melt experiments. Geology 41 (8), 851–854.
Friedman, I., Gleason, J., Sheppard, R.A., Gude, A.J., 1993a. Deuterium fractionation as water diffuses into silicic volcanic ash. Clim. Chang. Cont. Isot. Rec. 321–323.
Friedman, I., Gleason, J., Warden, A., 1993b. Ancient climate from deuterium content of water in volcanic glass. Clim. Chang. Cont. Isot. Rec. 309–319.
Friedman, I., Smith, R.L., D LONG, W., 1966. Hydration of natural glass and formation of perlite. Geol. Soc. Am. Bull. 77 (3), 323–328.
Gazis, C., Taylor, H.P., Hon, K., Tsvetkov, A., 1996. Oxygen isotopic and geochemical evidence for a short-lived, high-temperature hydrothermal event in the Chegem caldera, Caucasus Mountains, Russia. J. Volcanol. Geotherm. Res. 73 (3-4), 213–244.
Griggs, R.F., 1922. The Valley of Ten Thousand Smokes. National Geographic Society.
Gudmundsson, M.T., Sigmundsson, F., Björnsson, H., 1997. Ice-volcano interaction of the 1996 Gjálp subglacial eruption, Vatnajökull, Iceland. Nature 389 (6654), 954–957.
Hildreth, W., Fierstein, J., 2012. The Novarupta-Katmai eruption of 1912: largest eruption of the twentieth century: centennial perspectives. Geological Survey (USGS).1791.
Holt, E.W., Taylor, H.P., 2001. 18O/16O studies of fossil fissure fumaroles from the Valley of Ten Thousand Smokes, Alaska. Bull. Volcanol. 63 (2), 151–163.
Hudak, M.R., Bindeman, I.N., 2018. Conditions of pinnacle formation and glass hydration in cooling ignimbrite sheets from H and O isotope systematics at Crater Lake and the Valley of Ten Thousand Smokes. Earth Planet. Sci. Lett. 500, 56–66.
Jouzel, J., Masson-Delmotte, V., Cattani, O., Dreyfus, G., Falourd, S., Hoffmann, G., Minster, B., Nouet, J., Barnola, J.-M., Chappellaz, J., et al. 2007. Orbital and millennial antarctic climate variability over the past 800,000 years. Science 317 (5839), 793–796.
Keating, G.N., 2005. The role of water in cooling ignimbrites. J. Volcanol. Geotherm. Res. 142 (1), 145–171.
Kennett, J.P., Thunell, R.C., 1977. On explosive Cenozoic volcanism and climatic implications. Science 196 (4295), 1231–1234.
Lisiecki, L.E., Raymo, M.E., 2005. A Pliocene-Pleistocene stack of 57 globally distributed benthic δ18O records. Paleoceanography 20 (1).
Loewen, M.W., Bindeman, I.N., Melnik, O.E., 2017. Eruption mechanisms and short duration of large rhyolitic lava flows of Yellowstone. Earth Planet. Sci. Lett. 458, 80–91.
Mason, B.G., Pyle, D.M., Oppenheimer, C., 2004. The size and frequency of the largest explosive eruptions on Earth. Bull. Volcanol. 66 (8), 735–748.
Masson-Delmotte, V., Hou, S., Ekaykin, A., Jouzel, J., Aristarain, A., Bernardo, R., Bromwich, D., Cattani, O., Delmotte, M., Falourd, S., et al. 2008. A review of Antarctic surface snow isotopic composition: observations, atmospheric circulation, and isotopic modeling. J. Clim. 21 (13), 3359–3387.
Matthews, N.E., Vazquez, J.A., Calvert, A.T., 2015. Age of the Lava Creek supereruption and magma chamber assembly at Yellowstone based on 40Ar/39Ar and U-Pb dating of sanidine and zircon crystals. Geochem. Geophys. Geosyst. 16 (8), 2508–2528.
Miller, T.P., Smith, R.L., 1987. Late quaternary caldera-forming eruptions in the eastern Aleutian arc, Alaska. Geology 15 (5), 434–438.
Newman, S., Lowenstern, J.B., 2002. Volatilecalc: a silicate melt-H_2O-CO_2 solution model written in Visual Basic for Excel. Comput. Geosci. 28 (5), 597–604.
Nolan, G.S., Bindeman, I.N., 2013. Experimental investigation of rates and mechanisms of isotope exchange (O, H) between volcanic ash and isotopically labeled water. Geochim. Cosmochim. Acta 111, 5–27.
Pack, A., Herwartz, D., 2014. The triple oxygen isotope composition of the earth mantle and understanding δO17 variations in terrestrial rocks and minerals. Earth Planet. Sci. Lett. 390, 138–145.
Parrenin, F., Barnola, J.-M., Beer, J., Blunier, T., Castellano, E., Chappellaz, J., Dreyfus, G., Fischer, H., Fujita, S., Jouzel, J., et al. 2007. The EDC3 chronology for the EPICA Dome C ice core. Clim. Past 3 (3), 485–497.
Petit, J.-R., Jouzel, J., Raynaud, D., Barkov, N.I., Barnola, J.-M., Basile, I., Bender, M., Chappellaz, J., Davis, M., Delaygue, G., et al. 1999. Climate and atmospheric history of the past 420,000 years from the Vostok ice core, Antarctica. Nature 399 (6735), 429.
Pierce, K.L., 2003. Pleistocene glaciations of the Rocky Mountains. Dev. Quat. Sci. 1, 63–76.
Richmond, G.M., 1986. Stratigraphy and chronology of glaciations in Yellowstone National Park. Quat. Sci. Rev. 5, 83–98.
Sarna-Wojcicki, A., Morrison, S.D., Meyer, C., Hillhouse, J., 1987. Correlation of upper Cenozoic tephra layers between sediments of the western United States and eastern Pacific Ocean and comparison with biostratigraphic and magnetostratigraphic age data. Geol. Soc. Am. Bull. 98 (2), 207–223.
Scott, D.H., Tanaka, K.L., 1982. Ignimbrites of Amazonis Planitia region of Mars. J. Geophys. Res. Solid Earth 87 (B2), 1179–1190.
Seligman, A.N., Bindeman, I., Van Eaton, A., Hoblitt, R., 2018. Isotopic insights into the degassing and secondary hydration of volcanic glass from the 1980 eruptions of Mount St. Helens. Bull. Volcanol. 80 (4), 37.
Seligman, A.N., Bindeman, I.N., Watkins, J.M., Ross, A.M., 2016. Water in volcanic glass: from volcanic degassing to secondary hydration. Geochim. Cosmochim. Acta 191, 216–238.
Sharp, Z., Gibbons, J., Maltsev, O., Atudorei, V., Pack, A., Sengupta, S., Shock, E., Knauth, L., 2016. A calibration of the triple oxygen isotope fractionation in the SiO_2-H_2O system and applications to natural samples. Geochim. Cosmochim. Acta 186, 105–119.
Sheridan, M.F., 1970. Fuarmolic mounds and ridges of the Bishop Tuff, California. Geol. Soc. Am. Bull. 81 (3), 851–868.
Singer, B.S., Jicha, B.R., Condon, D.J., Macho, A.S., Hoffman, K.A., Dierkhising, J., Brown, M.C., Feinberg, J.M., Kidane, T., 2014. Precise ages of the Réunion event and Huckleberry Ridge excursion: episodic clustering of geomagnetic instabilities and the dynamics of flow within the outer core. Earth Planet. Sci. Lett. 405, 25–38.
Smellie, J.L., Edwards, B.R., 2016. Glaciovolcanism on Earth and Mars. Cambridge University Press.
Smith, R.B., Siegel, L.J., 2000. Windows into the Earth: The Geologic Story of Yellowstone and Grand Teton National Parks. Oxford University Press.
Squyres, S.W., Wilhelms, D.E., Moosman, A.C., 1987. Large-scale volcano-ground ice interactions on Mars. Icarus 70 (3), 385–408.
Tuffen, H., Owen, J., Denton, J., 2010. Magma degassing during subglacial eruptions and its use to reconstruct palaeo-ice thicknesses. Earth Sci. Rev. 99 (1), 1–18.
Vazquez, J.A., Stelten, M., Bindeman, I.N., Cooper, K.M., 2017. A field trip guide to the petrology of Quaternary volcanism on the Yellowstone Plateau. Tech. rep.. US Geological Survey.,
Wilson, C.J., Hildreth, W., 1997. The Bishop Tuff: new insights from eruptive stratigraphy. J. Geol. 105 (4), 407–440.
Wotzlaw, J.-F., Bindeman, I.N., Stern, R.A., DAbzac, F.-X., Schaltegger, U., 2015. Rapid heterogeneous assembly of multiple magma reservoirs prior to Yellowstone supereruptions. Sci. Rep. 5,
Zhang, Y., Behrens, H., 2000. H_2O diffusion in rhyolitic melts and glasses. Chem. Geol. 169 (1), 243–262.
Zheng, Y.-F., 1993. Calculation of oxygen isotope fractionation in hydroxyl-bearing silicates. Earth Planet. Sci. Lett. 120 (3-4), 247–263.
Zheng, Y.-F., et al. 1993. Calculation of oxygen isotope fractionation in anhydrous silicate minerals. Geochim. Cosmochim. Acta 57, 1079.